7 SCIENTIFIC HIGHLIGHT OF THE MONTH: Correlation effects in transition metals and their alloys studied by the fully self consistent KKR+DMFT method

---

Correlation effects in transition metals and their alloys studied by the fully self consistent KKR+DMFT method

Ján Minár

Universität München, Department of Chemistry, Physical Chemistry
Butenandtstr. 5-13, D-81377 München, Germany

Abstract

Recent results on magnetic and spectroscopic properties of transition metals, alloys and their surfaces, which were obtained by the LSDA+DMFT approach will be reviewed in this article. We exploit the various advantageous features offered by a LSDA+DMFT implementation on the basis of the KKR band structure method. This fully self consistent approach, with respect to charge and self-energy, allows to investigate in a most realistic way the impact of correlation effects in ordered as well as disordered systems. For the latter case the coherent potential approximation (CPA) is exploited. The fully-relativistic formulation implemented for space filling potentials gives the opportunity to study various ground state properties as for example orbital magnetic moments or total energies. Experimentally, the most detailed information on the electronic properties of correlated materials can be accessed by means of angle-resolved photoemission and inverse photoemission. In several earlier studies the measured spectra were described either within a single-particle approach based on the local spin density approximation, including matrix-element- and surface effects within so called one-step model or by sophisticated many-body approaches neglecting these effects. Here, we demonstrate that the combination of the one-step model with the LSDA+DMFT gives a detailed insight and the most stringent comparison between theory and corresponding experimental data.

1 Introduction

Density functional theory (DFT) is the state of the art technique for calculating the electronic and magnetic properties of a wide spectrum of systems ranging from atoms and molecules to surfaces and solids [1]. Its successes in treating the many-body problem is mainly due to the virtues of the local spin density approximation (LSDA) [2–4]. However, in spite of numerous impressive success it faces serious difficulties for strongly correlated materials such as Mott insulators, heavy fermion systems, high-temperature superconductors and many others. Nowadays, there exist various ways to improve the rather simple but successful LSDA. One way is to stay within the DFT formalism and to develop improved exchange correlation functionals like, for example, generalized gradient approximation (GGA) based functionals [5], orbital dependent functionals based on the optimized potential (OEP) method [**?**, 7] or self-interaction correction (SIC) [8] derived functionals. In order to determine excitation spectra quantitatively, time dependent DFT has been developed, but in practice the exchange-correlation kernel based on LSDA is still of limiting applicability.

To include many-body effects beyond LSDA and to describe different types of excitations, various many-body techniques have been developed. One of the most successful approaches is the dynamical mean field theory (DMFT) [9] that was introduced about 20 years ago. Within this approach more or less all local correlation effects like the Mott insulating state or quasiparticle excitations have been successfully described. The only approximation made within the DMFT in its standard formulation is the neglect of non-local, spatial correlations. In practice the DMFT has been primarily applied to solve various model Hamiltonians with limiting applicability to the real materials.

To go beyond the level of a model-like treatment and to investigate real materials with strong correlation effects a combination of DFT based methods supplemented by many-body theories have been suggested. In practice this leads to a complex, energy-dependent and non-local self-energy which has to be combined coherently into the existing DFT based methods by means of the Dyson equation for the Green's function. As a consequence, this combination allows for a realistic description of one-particle excitations in correlated systems. As an example, let us mention the GW-approximation [10] well suited for the case of insulators and semiconductors. Another approach is to consider Hubbard-type models where Coulomb-type interaction terms are included explicitly, which are assumed to be treated insufficiently within LSDA. Already the simplest Hartree-Fock like realization of such an approach called LSDA+U [11] scheme allows one to improve considerably the description of strongly correlated materials. Later on more advanced methods that represent correlation effects in terms of a complex and energy-dependent self-energy have been proposed. For example, the so called 3-body scattering method (3BS) [12] has been developed, which in principle is very well suited for the description of photoemission. Without any doubts, nowadays, the most successful approach consists in a combination of DFT with DMFT, the so called LSDA+DMFT method, that was developed during the last ten years or so (for reviews see [13, 14]). In spite of impressive progress in the development and application of the LSDA+DMFT method this framework has still to be improved. Recently Albers et al. [15] critically reviewed various issues connected with the LSDA+DMFT. In particular, to turn the LSDA+DMFT into a *method with predictive power for strongly correlated materials* [1] various important problems have to be solved, for example a fully self consistent coherent interface between LSDA and DMFT, reliable calculations of the Coulomb parameter U, the choice of the correlated orbitals, reliable DMFT impurity solvers applicable to a wide range of systems. In addition, a comparison to various spectroscopic properties is an important tool to check the achievements of theoretical developments. Concerning this, however, often only the pure spectral function is compared with experiment ignoring spectroscopic specific issues like e.g. matrix elements.

The aim of this contribution is to review the various advantageous features of the LSDA+DMFT implementation within the multiple scattering Korringa-Kohn-Rostoker (KKR) method [16]. This

---

[1] This words have been borrowed from the title of new collaborative Research Unit FOR1346 (funded by German DFG). The main general objective is to ultimately create a new standard of computational electronic structure schemes beyond LDA on a level which is suitable to predict and compute the properties of complex, correlated materials.

approach has been developed because the KKR method [17] represents the electronic structure by the corresponding single-particle Green's function leading to a number of attractive features of this scheme. In particular, several of the above mentioned questions could be addressed within the present approach. In Sec. 2 a combination of the LSDA+DMFT with the KKR band structure method is discussed. Various calculations of ground state properties are shown in Sec. 3.1.1. The second part of this review is devoted to the calculation of angle-resolved photoemission within so called one-step model including in particular more or less all relevant spectroscopy issues like, e.g. matrix elements and surface effects. Recent technical developments allow to perform calculations for ordered as well as of chemically disordered systems including electronic correlation effects. This topic is presented in Secs. 2.2.4 and 3.2.2.

2 Theory

In the late 1980s the dynamical mean field theory (DMFT) became a very important concept when dealing with many body Hubbard Hamiltonians for solids. Within the DMFT the infinite interacting many body lattice problem is mapped onto a single quantum impurity exposed to a mean field given by an effective bath. This central concept of the standard DMFT becomes exact in the limit of high lattice coordination number [18]. As a consequence of the DMFT equations for the on-site complex energy dependent self-energy and fully interacting Green's function these has to be calculated self consistently. Within this approach, even when dealing with a model Hubbard Hamiltonian, a lot of insight for example into the Mott-Hubbard transition has been obtained [9]. However, it has also been realized that in order to calculate the electronic structure properties of realistic materials the combination of the LSDA with the DMFT is desirable. First successful steps in this direction had been done by Anisimov et al. [19] and Katsnelson et al. [20]. In the LSDA+DMFT the local one particle Green's function needed as an input to the DMFT self consistent cycle is obtained from the LSDA method. Up to now most of the LSDA+DMFT implementations (see for example reviews [13, 14] and references given there) have been performed using only DMFT self consistency. This means the LSDA charge density and consequently the effective LSDA potential has been fixed. Therefore, one neglects the impact of correlation effects on the charge distribution. Until now only few completely self consistent schemes, e.g. with respect to charge density and self-energy, have been proposed and implemented. To underline the importance of the complete LSDA+DMFT self consistency we mention the problem of phase diagram calculations and localization in f-electron systems [21, 22], the description of non-quasiparticle states in the Heusler alloys [23] and the problem to describe angle-integrated [24] and angle-resolved photoemission of 3d-ferromagnets [25]. The first fully self consistent implementations of the LSDA+DMFT have been done on the basis of the linear muffin tin orbital method (LMTO) [21], followed by the EMTO method [26]. One of the first self consistent schemes based on a full potential scheme has been proposed by Minar et al. [16] for the KKR Green's function method. Most of the work done by the LSDA+DMFT method deals with electronic and magnetic properties of strongly correlated materials. However, correlation effects are also often of crucial importance to describe the cohesive energy, the equilibrium lattice constant and the bulk modulus as demonstrated for the case of plutonium [22, 27] and cerium [28]. After these first experiences, the need for more systematic implementations and investigations on numerical problems of LSDA+DMFT emerged.

A very detailed study of the effects of self- consistency on the total energy has been presented by Pourovskii et al. [29]. In spite of various numerical problems, recently, the huge potential of the LSDA+DMFT method concerning total energies has been demonstrated. For example, the collapse of the magnetic moment of MnO [30], equilibrium volume and bulk modulus of Ni and Mn [31] or correlation driven structural properties of complex materials like $KCuF_3$ and $LaMnO_3$ [32] had been discussed.

In this section we briefly review a full potential KKR implementation of the DMFT theory. We will discuss the various advantages of this approach like, for example, fully self-consistency, the total energy problem and the combination of the LSDA+DMFT with the coherent potential approximation and its fully relativistic extension. In addition, the combination of the DMFT with the one step model of photoemission allows for a direct comparison to the angle-resolved photoemission of ordered as well as of disordered systems including matrix elements, final state and surface effects.

2.1 Formulation of the problem

All standard approaches for a realistic electronic structure calculation of strongly correlated materials start from a choice of the set of orbitals that are not accurately described enough within the standard DFT LSDA method. We call them "correlated orbitals" and indicate them with $\phi_i^n(\vec{r})$, where n specifies the Bravais lattice site and the i is an index that enumerates the orbitals within the unit cell of the crystal. The choice of "correlated orbitals" is dictated by physical motivations for the problem under consideration and always implies some degree of arbitrariness. Usually the correlated orbitals are derived from d or f atomic states and the index i stands for the atomic quantum numbers l, m, σ. Natural choices can be the Linear Muffin-Tin Orbitals [22] or the Wannier functions [33, 34] or downfolded orbitals constructed via NMTO approach [35].

After having decided for the set of "correlated orbitals", we correct the standard DFT LSDA Hamiltonian with an additional Hubbard interaction term [13] that explicitly accounts for the local Coulomb repulsion for the orbitals in the set:

$$H = H_{LSDA} + H_U - H_{DC} \ . \tag{1}$$

Here H_{LSDA} stands for the ordinary LSDA Hamiltonian, H_U describes the additional effective electron-electron interaction and the one-particle Hamiltonian H_{DC} serves to eliminate double counting of the interactions already accounted for by H_{LSDA}. H_{DC} used in our implementation for transition metals and compounds will be discussed later in Sec. 2.2. Similar to the LSDA+U method [11], this many-body Hamiltonian is specified by a number of parameters representing Coulomb matrix elements. Among these parameters the Hubbard U that represents the screened on-site Coulomb interaction is the most important one. Accordingly, several schemes have been suggested in the literature to determine U from LSDA calculations [14, 36]. However, in this work we use it as a parameter. The resulting many-particle Hamiltonian can not be diagonalized exactly, thus various methods were developed in the past to find an approximate solution [9]. Among them one of the most promising approaches is to deal with Eq. (1) within the DMFT.

The main idea of DMFT is to map a periodic many-body problem onto an effective single-impurity problem that has to be solved self consistently. For this purpose one describes the electronic properties of the system in terms of the one particle Green's function $\hat{G}(E)$, being the solution of the equation:

$$[E - \hat{H}_{LSDA} - \hat{\Sigma}(E)]\hat{G} = \hat{1} \ , \tag{2}$$

where E is the complex energy and the effective self-energy operator $\hat{\Sigma}$ is assumed to be a single-site quantity for site n:

$$\hat{\Sigma}(E) = \sum_{ij} |\phi_{ni}\rangle \Sigma_{ij}(E) \langle \phi_{nj}| \ . \tag{3}$$

Within DMFT, the self-energy matrix $\Sigma_{ij}(E)$ is a solution of the many-body problem of an impurity placed in an effective medium. This medium is described by the so called *bath* Green's function matrix $\mathcal{G}$ defined as:

$$\underline{\mathcal{G}}^{-1}(E) = \underline{G}^{-1}(E) + \underline{\Sigma}(E) \ , \tag{4}$$

with the underline indicating matrices with respect to orbital index i. The Green's function matrix $G_{ij}(E)$ is calculated as a projection of $\hat{G}(E)$ onto the impurity site:

$$G_{ij}(E) = \langle \phi_i^n | \hat{G}(E) | \phi_j^n \rangle \ . \tag{5}$$

Because the self-energy $\Sigma_{ij}(E)$ depends on the *bath* Green's function $\mathcal{G}_{ij}(E)$ the DMFT equations have to be solved self consistently. From a technical point of view the problem can be split into two parts. One is dealing with the solution of Eq. (2) and the second one is the effective many-body problem to find the self-energy $\Sigma_{ij}(E)$ according to Eq. (4). Within the present work, the first task is solved by the KKR band structure method, as described below in Sec. 2.2. The choice and details of solving the many-body effective impurity problem, often referred to as DMFT-solver, can be found in various LSDA+DMFT reviews for example [13, 14].

2.2 Multiple scattering implementation of the LSDA+DMFT method

In the following section we shortly review a fully self consistent (with respect to charge density and self-energy) LSDA+DMFT implementation within the full potential fully relativistic multiple scattering Korringa Kohn Rostoker (KKR) method [16]. This approach was motivated because the KKR method represents the electronic structure by the corresponding single-particle Green's function leading therefore to a number of very attractive features of the scheme that are exploited in the subsequent work [2]. This allows to combine the KKR method with the DMFT straightforwardly. In addition, an outstanding feature of the KKR method is the possible use of the Dyson equation which relates the Green's function of a perturbed system with the Green's function of the corresponding unperturbed reference system. Using the Dyson equation allows to calculate various properties of low dimensional systems like e.g. semi infinite 2D-surfaces, nano-structures or embedded 3D- or 2D- systems. In addition, the KKR Green's function method allows to deal with substitutional disordered alloys in the framework of the coherent potential approximation (CPA) [37].

---

[2] For a recent review where various advantages of the KKR method are listed see Ψ_k highlight of the month [17] and references therein.

The idea of the LSDA+DMFT approach presented here is to account for the general non-local, site-diagonal, complex and energy-dependent self-energy Σ^{DMFT} into the KKR method already when calculating the basis functions, i.e. when solving the single site Schrödinger (or Dirac) equation. This allows directly to exploit all features of the KKR Green's function method within LSDA+DMFT calculations and consequently allows to quantitatively account for correlation effects.

As already mentioned, there are various approaches available to combine the LSDA with the DMFT method [13, 14]. In most implementations as a first step the corresponding LSDA problem is solved variationally using a given basis set (e.g. LMTO). The corresponding local Green's function is determined by the spectral representation of the Kohn-Sham Hamiltonian. The resulting local self-energy Σ^{DMFT} and local Green's function can be in turn used to calculate a new charge density and an effective LSDA potential. However, in order to combine coherently the LSDA with the DMFT method (in the spirit of spectral density functional theory [22]) one needs to solve self consistently the following Dyson equation:

$$\begin{aligned} G(\vec{r},\vec{r}\,',E) &= G_0(\vec{r},\vec{r}\,',E) \\ &+ \int \mathrm{d}^3r'' \int \mathrm{d}^3r''' G_0(\vec{r},\vec{r}\,'',E) \left[V_{\mathrm{eff}}(\vec{r}\,'')\delta(\vec{r}\,''-\vec{r}\,''') + \Sigma(\vec{r}\,'',\vec{r}\,''',E)\right] G(\vec{r}\,''',\vec{r}\,',E), \end{aligned} \quad (6)$$

where $G_0(\vec{r},\vec{r}\,'',E)$ is the free electron Green's function. The potential $V_{\mathrm{LSDA}}(\vec{r})$ denotes the (effective) potential (in the relativistic spin DFT defined as $V_{\mathrm{eff}}(\vec{r}) = [\overline{V}_{\mathrm{eff}}(\vec{r}) + \beta\boldsymbol{\sigma}\mathbf{B}_{\mathrm{eff}}(\vec{r})]$ where $\overline{V}_{\mathrm{eff}}(\vec{r})$ denotes the spin-independent potential, and $\mathbf{B}_{\mathrm{eff}}(\vec{r})$ is the magnetic field [38]). β and $\boldsymbol{\alpha}$ used below are standard Dirac matrices with the latter one given by $\alpha_k = \sigma_x \otimes \sigma_k$ $(k = x, y, z)$ in terms of the 2×2 Pauli-matrices σ_k.

A very efficient way to solve Eq. (6) is offered by the multiple scattering KKR method. Having decomposed the system into atomic regions (Wigner-Seitz-cells) and considering that Σ^{DMFT} is an on-site quantity the equation can be solved using the standard KKR formalism. This implies that first one must solve the so-called single site scattering problem to obtain the single site t-matrix and the corresponding scattering wave function $\Psi(\vec{r})$. In the relativistic spin density functional theory [1, 39] the corresponding single site Dirac equation reads:

$$\left[\frac{\hbar}{i}c\vec{\alpha}\cdot\vec{\nabla} + \beta mc^2 + V_{\mathrm{eff}}(\vec{r}) + \int d^3r'\Sigma(\vec{r},\vec{r}\,',E)\right]\Psi(\vec{r}) \;=\; E\Psi(\vec{r})\,. \quad (7)$$

Here, the $\Psi(\vec{r})$ are four-component spinor functions with corresponding energies E. To be able to solve Eq. (7) one makes the following ansatz for the wave function $\Psi = \sum_\Lambda \Psi_\Lambda$, with the combined relativistic quantum number $\Lambda = (\kappa, \mu)$. In addition, in the spirit of the DMFT $\Sigma(\vec{r},\vec{r}\,',E)$ one has to project onto the localized set of orbitals $\phi^n_\Lambda(\vec{r})$. The corresponding matrix $\Sigma_{\Lambda,\Lambda'}(E)$ is obtained as an output of the DMFT solver. In practice, $\Sigma_{\Lambda\Lambda'}(E)$ is used only for correlated d- or f- orbitals (see above). It is worth to note that even in the case of the spherical muffin-tin or atomic sphere approximation to the potential, full-potential like coupled Eqs. (7) have to be solved. This implies that the full-potential version of the KKR has to be used. After having solved the set of coupled equations for the wave functions one gets the corresponding single site t matrix by standard matching to the Hankel and Bessel functions as free electron solutions. When solving the single-site problem, obviously the entire complexity of the underlying complex non-local potential within LSDA+DMFT is accounted for. Accordingly, the resulting regular and irregular scattering wave functions $Z_\Lambda(\vec{r},E)$ and $J_\Lambda(\vec{r},E)$ as well as the corresponding single-site t-matrix carry all information on the underlying LSDA+DMFT Hamiltonian. This means that in contrast to other LSDA+DMFT implementations, the effect of the self-energy is also reflected in the wave functions Ψ. This becomes important, for example, in a total energy calculation and for the photoemission matrix elements (see Sec. 2.2.4).

With the single-site t matrix available the next step of the KKR calculation is to solve the multiple scattering problem. This task can be done by using the scattering path operator τ [17] and it is independent from the DMFT. For a finite system this can be done straight forwardly by inverting the so called KKR-matrix, $\underline{\underline{\tau}}(E) = [\underline{\underline{t}}(E)^{-1} - \underline{\underline{G}}_0(E)]^{-1}$ with the double underline indicating matrices with respect to site and spin-angular (Λ) character. Dealing with a three-dimensional periodic system this equation can also be solved exactly by Fourier transformation. As a result the retarded site diagonal Green's function $G(\vec{r},\vec{r}\,',E)$ can be written as [37, 40]:

$$\begin{aligned} G(\vec{r},\vec{r}\,',E) &= \sum_{\Lambda,\Lambda'} Z_\Lambda(\vec{r},E)\tau^{nn}_{\Lambda,\Lambda'}(E)Z^\times_{\Lambda'}(\vec{r}\,',E) \\ &- \sum_{\Lambda}\{Z_\Lambda(\vec{r},E)J^\times_\Lambda(\vec{r}\,',E)\Theta(\vec{r}\,'-\vec{r}) \\ &+ J_\Lambda(\vec{r},E)Z^\times_\Lambda(\vec{r}\,',E)\Theta(\vec{r}-\vec{r}\,')\} \,, \end{aligned} \tag{8}$$

where $\vec{r}$ ($\vec{r}\,'$) lies in the atomic cell n representing cell-centered coordinates and × indicates a so-called left-hand side solution [41]. With the Green's function $G(\vec{r},\vec{r}\,',E)$ available all properties of interest as e.g. , the charge density, can be calculated straight forwardly and in this way the calculated Green's function G includes all effects of the self-energy Σ^{DMFT}. The definition of the Green's function and the expressions given above are not restricted to real energies E but also holds for arbitrary complex energies z. The fact that $G(\vec{r},\vec{r}\,',E)$ is analytical [42] allows, in particular, to perform the energy integration for the charge density on a contour in the complex energy plane [43,44] with typically around 30 energy mesh points. On the other hand the self-energy Σ^{DMFT} is often calculated for a mesh of Matsubara frequencies. This implies that it is necessary to use analytical continuation techniques to transform Σ^{DMFT} from Matsubara frequencies ω onto the KKR complex energy contour. It is worth to note that in general Σ^{DMFT} is not Hermitian and for low symmetry systems one has to consider right and left handed solutions of (7) when constructing the Green's function $G(\vec{r},\vec{r}\,',E)$ [41].

In order to construct the bath Green's function needed as the input of the DMFT solver, the localized Green's function is calculated by projecting the total Green's function onto the correlated atomic site. This is done by projecting $G(\vec{r},\vec{r}\,',E)$ with a localized set of orbitals $\phi_\Lambda(\vec{r})$:

$$G_{\Lambda\Lambda'}(E) = \int d^3r \int d^3r\,'\phi_\Lambda(\vec{r})G(\vec{r},\vec{r}\,',E)\phi_{\Lambda'}(\vec{r}\,') \,. \tag{9}$$

The multiple scattering formalism provides the natural choice of the projectors $\phi_\Lambda(\vec{r})$ which are the regular single-site solutions of the Kohn-Sham-Dirac equations. For transition metal systems only the d-d sub-block of the $\underline{G}^{nn}(E)$ is considered with $\phi_\Lambda(\vec{r})$ wave functions with $l = 2$. In principle the choice of the $\phi_\Lambda(\vec{r})$ is arbitrary as long as $\phi_\Lambda(\vec{r})$ is a complete set of functions. This implies that a localized basis set is calculated at a given reference energy E_{ref} (set to be the center of gravity of the occupied d- or f-band) with the magnetic field set to zero in the relativistic case. In

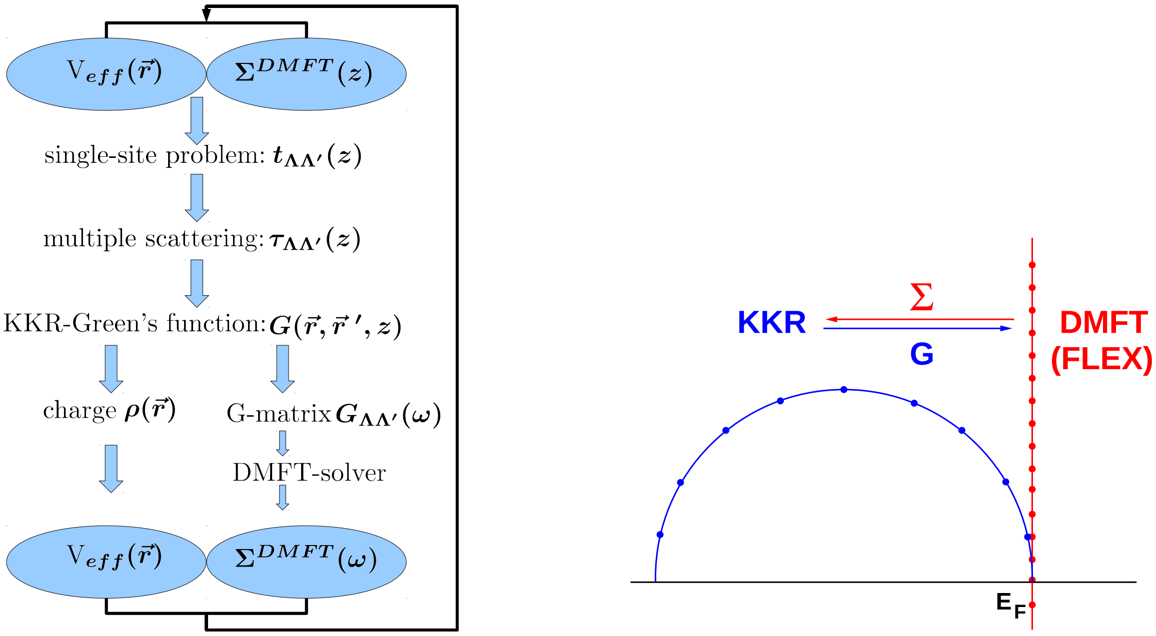

Figure 1: Left: Schematic overview of the KKR+DMFT scheme. Right: Illustration of the energy paths involved. The blue semicircle is the complex energy path used by KKR to calculate the charge density. After the bath Green's function G is obtained, it is analytically continued onto the imaginary axis (red) to calculate the self-energy Σ^{DMFT} via the DMFT impurity solver. The latter is analytically extrapolated back to the semicircle.

the full-potential case couplings to the other l-channels as a consequence of crystal symmetry have to be suppressed.

Finally, a description of the flow diagram of the self consistent LSDA+DMFT approach is presented in Fig. 1. Eq. (7) provides the set of regular (Z) and (J) irregular solutions of the single-site problem. Together with the t matrix and the scattering path operator τ the KKR Green's function is constructed from Eq. (8). To solve the many-body problem the projected impurity Green's function is constructed according to Eq. (9). The LSDA Green's function $G_{\Lambda\Lambda'}(E)$ is calculated on the complex contour which encloses the valence band one-electron energy poles. The Padé analytical continuation scheme is used to map the complex local Green's function $G_{\Lambda\Lambda'}(E)$ on the set of Matsubara frequencies or real axis, respectively, which is used when dealing with the many-body problem. In the current fully relativistic implementation the perturbative SPTF (spin-polarized T-matrix + FLEX) [45] as well as $T = 0K$ spin-polarized T-matrix [46] solvers of the DMFT problem are used. In fact any DMFT solver could be included which supplies the self-energy $\Sigma(E)$ as a solution of the many-body problem. The Padé analytical continuation is used once more to map back the self-energy from the Matsubara axis to the complex plane, where the new KKR Green's function is calculated. As was described in the previous sections, the key role is played by the scattering path operator $\tau^{nn}_{\Lambda\Lambda'}(E)$, which allows us to calculate the charge in each SCF iteration and the new potentials that are used to generate the new single particle Green's function.

Of course double counting corrections H_{DC} have to be considered explicitly. The problem of the double-counting correction is definitely one of the main challenges towards first-principle calculations within LSDA+DMFT. Until know various schemes for double counting correction have been suggested [14]. The simplest choice, i.e. the idea of the static LSDA+U scheme has been used here. We apply the double counting corrections to the self-energy when solving the many-body problem. In the case of metallic transition metals, their compounds and alloys the so called around mean field (AMF) double counting correction seems to be most appropriate. It is worth to note here, that until now it is more or less impossible to derive an exact analytical equation for the double counting correction. An alternative way to get an exact solution of the double counting problem seems to be possible on the level of the GW+DMFT scheme [47]. Therefore, it is important to use a comparison to angle-resolved photoemission (ARPES) experiments as a stringent criterium for the choice of the optimal H_{DC}. However, to be able to make a decision between various suggestions for H_{DC} it is helpful to calculate not only the bare spectral function, e.g. ImG, but instead to perform a complete photoemission calculation. (for example with the one step model of photoemission, see Sec. 2.2.4). In fact, using the one step model of photoemission one can clearly see that the AMF H_{DC} is an appropriate choice for at least transition metals [25, 48, 49].

2.2.1 LSDA+DMFT treatment of disordered alloys

An outstanding feature of the KKR method is the Dyson equation relating the Green's function of a perturbed system with the Green's function of the corresponding unperturbed reference system. Because of this property, the KKR Green's function method allows to deal with substitutional disorder including both diluted impurities and concentrated alloys in the framework of the CPA [50, 51]. Within this approach (KKR-CPA) the propagation of an electron in an alloy is regarded as a succession of elementary scattering processes due to random atomic scatterers, with an average taken over all configurations of the atoms. This problem can be solved assuming that a given scattering center is embedded in an effective medium whose choice is open and can be determined in a self consistent way. The physical condition corresponding to the CPA is simply that a single scatterer embedded in the effective CPA medium should produce no further scattering on the average. A similar philosophy is applied also when dealing with many-body problems for crystals in the framework of DMFT. Thus it seems to be rather natural to combine the DMFT and KKR-CPA method. In fact the combination of the KKR-CPA for disordered alloys and the DMFT scheme is based on the same arguments as used by Drchal et al. [52] when combining the LMTO Green's function method for alloys [53] with the DMFT.

The combination of the CPA and LSDA+DMFT turned out to be a quite powerful technique to calculate electronic structure properties of substitutionally disordered correlated materials [16, 54–56]. Within the CPA the configurationally averaged properties of a disordered alloy are represented by a hypothetical ordered CPA-medium, which in turn may be described by a corresponding site-diagonal scattering path operator τ^{CPA}, which in turn is closely connected with the electronic Green's function. For example for a binary system $\mathrm{A}_x\mathrm{B}_{1-x}$ composed of components A and B with relative concentrations x_{A} and x_{B} the corresponding single-site t-matrix t^{CPA} and the multiple scattering path operator τ^{CPA} are determined by the so called CPA-condition:

$$x_{\mathrm{A}}\tau^{\mathrm{A}} + x_{\mathrm{B}}\tau^{\mathrm{B}} = \tau^{\mathrm{CPA}}. \tag{10}$$

The above equation represents the requirement that embedding substitutionally an atom (of type A or B) into the CPA medium should not cause additional scattering. The scattering properties of an

A atom embedded in the CPA medium, are represented by the site-diagonal component-projected scattering path operator τ^{A} (angular momentum index omitted here)

$$\tau^{\mathrm{A}} = \tau^{\mathrm{CPA}} \left[1 + \left(t_{\mathrm{A}}^{-1} - t_{\mathrm{CPA}}^{-1}\right) \tau^{\mathrm{CPA}}\right]^{-1} \quad , \tag{11}$$

single-site matrices of the A component and of the CPA effective medium. A corresponding equation holds also for the B component in the CPA medium. The coupled sets of equations for τ^{CPA} and t^{CPA} have to be solved iteratively within the CPA cycle.

The above scheme can straightforwardly be extended to include the many-body correlation effects for disordered alloys [16]. Within the KKR approach the local multi-orbital and energy dependent self-energies ($\Sigma_A^{DMFT}(E)$ and $\Sigma_B^{DMFT}(E)$) are directly included into the single-site matrices t_A and t_B, respectively by solving the corresponding Dirac Eq. (7). Consequently, all the relevant physical quantities connected with the Green's function, as for example, the charge density contain the electronic correlations beyond the LSDA scheme.

2.2.2 Combination of the LSDA+DMFT with disordered local moment approach

In the following subsection we address the question to which extent a regime of strong correlations can be studied by means of an implementation suited to deal with moderately correlated systems. In particular the spin-polarized T-matrix fluctuation-exchange solver (SPTF) [45, 57] has been implemented to treat the problem of magnetic fluctuations in transition metals, and has been successfully applied to the ferromagnetic phases of Fe, Co, Ni [25, 57, 58] and to the antiferromagnetic phase of γ-Mn [59], as well as to half-metallic ferromagnets [23]. It is quite stable, computationally rather cheap and deals with the complete four-indices interaction matrix. On the other hand, its perturbative character restricts its use to relatively weakly, or moderately, correlated systems.

Not surprisingly, the SPTF performs well when starting from a spin-polarized solution, since the spin-splitting contains already the main part of the exchange and correlation effects. On the other hand, the direct application of SPTF to a non-magnetic reference state can create stability problems. This is because one tries to attribute the strong and essentially mean-field effect of the formation of a local magnetic moment to dynamical fluctuations around the non-spin-polarized state. This is fine when one uses the quantum monte carlo (QMC) method, which has no formal restrictions on the value of fluctuations, but seems problematic for the perturbative approaches. As a way to reduce such a limitation we propose a combination of SPTF with the disordered local moment (DLM) approach [60, 61]. As already shown for the case of actinides [62] the inclusion of the fluctuations of randomly oriented local moments can improve drastically the description of energetics in the paramagnetic phase. Therefore, one can hope that it allows us to extend the range of applicability of SPTF.

In DLM the itinerant electrons form self-maintaining "local moments" which are analogous - but physically different - to the localized spins of the Heisenberg model. With $\hat{\mathbf{e}}_i$ the orientations of the moments at the sites i, we can describe the system through the generalized grand-canonical potential $\Omega(\{\hat{\mathbf{e}}_i\})$. Then a mean-field approximation of the true potential is constructed as expansion around a single-site spin Hamiltonian [61]:

$$\Omega_0(\{\hat{\vec{e}}_i\}) = -\sum_i \vec{h}_i \hat{\vec{e}}_i . \tag{12}$$

The self consistent parameters h_i define a set of probabilities $P_i(\hat{\vec{e}}_i)$ of finding the moments oriented along $\hat{\vec{e}}_i$. Explicit calculations can now be made using standard methods developed for substitutionally disordered alloys, as the Coherent Potential Approximation (CPA), which is straightforwardly implemented within the multiple-scattering theory of KKR [16] (see above). The study of the paramagnetic phase is especially simple, since the problem can be reduced to a binary alloy, where the half of the sites are occupied by "up" moments and the other half by "down" moments.

2.2.3 Total energy calculations

In the Sec. 2.1 we have presented the equations that define the LSDA+DMFT scheme in terms of the local problem and a self consistent bath. These equations can be obtained by many different techniques [9], but in perspective of total energy calculations we have already adopted the point of view of the spectral density-functional theory of Savrasov and Kotliar [22]. In the case of the KKR implementation presented above the LSDA+DMFT total energy can be calculated from:

$$E_{LSDA+DMFT} = E_{LSDA}\left[\rho(\mathbf{r}), G(\omega)\right] - \langle H_U \rangle \ . \tag{13}$$

It should be noted that E_{LSDA}, in particular its band energy contribution, already contains the self-energy contribution and therefore the Galitskii-Migdal term has to be removed, since it is already added twice with the band energy.

The evaluation of Eq. (13) requires only the additional calculation of the Galitskii-Migdal energy, since the band energy results from the DFT part of the KKR code. While it might be simpler to evaluate the Galitskii-Migdal correction directly within the local problem (inside the DMFT solver integrating over Matsubara frequencies), we prefer to work again on the semicircular complex energy contour, retaining to the same formalism for both contributions of the total energy. This implies we calculate

$$\langle H_U \rangle = -\frac{1}{2\pi} \mathrm{Im} \sum_{\Lambda_1 \Lambda_2} \int dz\, \Sigma_{\Lambda_1 \Lambda_2}(z) G_{\Lambda_2 \Lambda_1}(z) \, . \tag{14}$$

The integration is performed over the contour starting close to the real energy axis at the bottom of a valence band and ending at the Fermi energy. It turned out that this procedure is numerically more stable than the evaluation of the Galitskii-Migdal correction using an integration over the Matsubara frequencies inside the DMFT solver.

2.2.4 Fully relativistic one-step model of photoemission for alloys

Spectroscopy is an extremely important experimental tool providing information on the electronic structure of the probed system that has to be seen as a stringent benchmark for the success of any electron structure theory. Photoemission spectroscopy (PES) or its inverse – the Bremsstrahlung isochromate spectroscopy (BIS) – in their angle-integrated form should reflect the density of states

(DOS) rather directly – in particular in the high photonenergy regime (XPS). For that reason it is quite common to check the DMFT-based calculations by comparing the calculated DOS directly to the PES spectra (see the reviews [13, 14, 63] for example).

However, this approach ignores the influence of the specific PES matrix elements that in general will introduce an element- and energy-dependent weight to the partial DOS. In case of angle-resolved photoemission (ARPES) the situation is even move severe as the surface as well as dipole selection rules may have a very pronounced impact on the spectra [64] demanding for a coherent description within the one-step model of photoemission [65]. To achieve a reliable interpretation of experiments, however, it is inevitable to deal with so-called matrix-element effects which considerably modify the raw spectrum. Above all, the wave-vector and energy dependence of the transition-matrix elements has to be accounted for. These issues are known to be important and actually cannot be neglected. They result from strong multiple-scattering processes which dominate the electron dynamics in the low-energy regime of typically 1-200 eV [66]. The transition-matrix elements also include the effects of selection rules which are not accounted for in the raw spectrum. Loosely speaking, it can be said that the main task of a theory of photoemission is to close the gap between the raw spectrum obtained by LSDA+DMFT electronic-structure calculations and the experiment. The most successful theoretical approach concerning this is the so-called one-step model of photoemission as originally proposed by Pendry and co-workers [66–68]. In the following a short overview will be given on the recent extensions of the one-step model which are connected with correlation effects and disordered alloys.

The main idea of the one-step model is to describe the actual excitation process, the transport of the photoelectron to the crystal surface as well as the escape into the vacuum [69] as a single quantum-mechanically coherent process including all multiple-scattering events. Within this model self-energy corrections, which give rise to damping in the quasi-particle spectrum, are properly included in both the initial and the final states. This for example allows for transitions into evanescent band gap states decaying exponentially into the solid. Similarly the assumption of a finite lifetime for the initial states gives the opportunity to calculate photoemission intensities from surface states and resonances. Treating the initial and final states within the fully relativistic version of layer KKR theory [70, 71], it is a straight forward task to describe complex layered structures like thin films and multilayers within the photoemission theory. Furthermore, the surface described by a barrier potential can be easily included into the multiple-scattering formalism as an additional layer. A realistic surface barrier model which shows the correct asymptotic behavior has been introduced, for example, by Rundgren and Malmström [72].

We start our considerations by a discussion of Pendry's formula for the photocurrent which defines the one-step model of PES [67]:

$$I^{\mathrm{PES}} \propto \mathrm{Im}\, \langle \epsilon_f, \mathbf{k}_{||} | G_2^+ \Delta G_1^+ \Delta^\dagger G_2^- | \epsilon_f, \mathbf{k}_{||} \rangle \, . \tag{15}$$

The expression can be derived from Fermi's golden rule for the transition probability per unit time [73]. Consequently, I^{PES} denotes the elastic part of the photocurrent. Vertex renormalizations are neglected. This excludes inelastic energy losses and corresponding quantum-mechanical interference terms [67, 73, 74]. Furthermore, the interaction of the outgoing photoelectron with the rest system is not taken into account. This "sudden approximation" is expected to be justified for not too small photon energies. We consider an energy-, angle- and spin-resolved photoemission experiment. The state of the photoelectron at the detector is written as $|\epsilon_f, \mathbf{k}_{\|}\rangle$, where $\mathbf{k}_{\|}$ is the component of the wave vector parallel to the surface, and ϵ_f is the kinetic energy of the photoelectron. The spin character of the photoelectron is implicit by included in $|\epsilon_f, \mathbf{k}_{\|}\rangle$ which is understood as a four-component Dirac spinor. The advanced Green function G_2^- in Eq. (15) characterizes the scattering properties of the material at the final-state energy $E_2 \equiv \epsilon_f$. Via $|\Psi_f\rangle = G_2^-|\epsilon_f, \mathbf{k}_{\|}\rangle$ all multiple-scattering corrections are formally included. For an appropriate description of the photoemission process we must ensure the correct asymptotic behavior of $\Psi_f(\mathbf{r})$ beyond the crystal surface, i. e. a single outgoing plane wave characterized by ϵ_f and $\mathbf{k}_{\|}$. Furthermore, the damping of the final state due to the imaginary part of the inner potential $iV_{0\mathrm{i}}(E_2)$ must be taken into account. We thus construct the final state within spin-polarized low-energy electron diffraction (SPLEED) theory considering a single plane wave $|\epsilon_f, \mathbf{k}_{\|}\rangle$ advancing onto the crystal surface. Using the standard layer-KKR method generalized for the relativistic case [65, 75], we first obtain the SPLEED state $-T\Psi_f(\mathbf{r})$. The final state is then given as the time-reversed SPLEED state ($T = -i\sigma_y K$ is the relativistic time inversion). Many-body effects are included phenomenologically in the SPLEED calculation, by using a parametrized, weakly energy-dependent and complex inner potential $V_0(E_2) = V_{0\mathrm{r}}(E_2) + iV_{0\mathrm{i}}(E_2)$ as usual [66]. This generalized inner potential takes into account inelastic corrections to the elastic photocurrent [73] as well as the actual (real) inner potential, which serves as a reference energy inside the solid with respect to the vacuum level [76]. Due to the finite imaginary part $iV_{0\mathrm{i}}(E_2)$, the flux of elastically scattered electrons is continuously reduced, and thus the amplitude of the high-energy wave field $\Psi_f(\mathbf{r})$ can be neglected beyond a certain distance from the surface.

For disordered alloys the CPA scheme can straightforwardly be extended to include the many-body correlation effects for disordered alloys [16]. According to the LSDA+DMFT approach realized in the framework of the fully relativistic SPR-KKR multiple scattering theory we use the self-energy $\Sigma_A^{DMFT}(E)$ calculated self consistently using dynamical mean field theory [9]. Within the KKR approach the local multi-orbital and energy dependent self-energies ($\Sigma_A^{DMFT}(E)$ and $\Sigma_B^{DMFT}(E)$) are directly included into the single-site matrices t_A and t_B, respectively by solving the corresponding Dirac Eq. (7). Consequently, all the relevant physical quantities connected with the Green's function and used for photoemission calculations, as for example, the matrix elements or scattering matrices like t^{CPA} contain the electronic correlations beyond the LSDA scheme. A detailed description of the generalized one-step model for disordered magnetic alloys can be found in [56]. Here we present the expression for the CPA photocurrent only. Following Durham *et al.* [77,78] we have to perform the configurational average of these different contributions to the photocurrent, leading to the fully relativistic expression:

$$\begin{aligned} < I^{\mathrm{PES}}(\epsilon_f, \mathbf{k}_{\|}) > &= < I^{\mathrm{a}}(\epsilon_f, \mathbf{k}_{\|}) > + < I^{\mathrm{m}}(\epsilon_f, \mathbf{k}_{\|}) > \\ &+ < I^{\mathrm{s}}(\epsilon_f, \mathbf{k}_{\|}) > + < I^{\mathrm{inc}}(\epsilon_f, \mathbf{k}_{\|}) > \\ &. \end{aligned} \tag{16}$$

When dealing with disorder in the alloys, an additional term I^{inc}, the so called "incoherent" term appears. This contribution to the alloy photocurrent appears because the spectral function of an disordered alloy [37] is defined as a non single-site quantity. In fact this contribution is closely connected with the presence of the irregular wave functions well-known from the spherical representation of the Green function G_1^+.

3 Applications

In this section we review some results that have been obtained using the LSDA+DMFT as implemented in the full-potential KKR method (2.2). The use of a fully relativistic formulation on the basis of the four-component Dirac formalism allows to deal with all spin-orbit coupling induced properties like for example orbital magnetic moments of ferromagnetic transition metals. Magnetic moments and other ground state properties will be discussed in Sec. 3.1.1. Investigations on ground states properties are complemented by investigations on spectroscopic properties with an emphasis on valence band photoemission calculated on the basis of the so-called one-step model. In Sec. 3.2.1 the spin-orbit coupling induced Fano effect observed in angle-integrated photoemission is discussed. To achieve more stringent and detailed information about the electronic structure of correlated materials, the calculation of ARPES is highly desirable. As already mentioned our approach combines coherently LSDA+DMFT and ARPES relevant issues: the surface geometry, final state effects and the transition matrix elements accounting for the selection rules. Examples will be shown for the low index surfaces of transition metals like Ni or Fe in Sec. 3.2.2) and for the disordered NiPd-alloy system in Sec. 3.2.3. In the last Sec. 3.3 recent developments of the KKR formalism concerning $\vec{k}$ dependent self-energies will be discussed for the case of the electron-phonon coupling.

3.1 Ground state properties

3.1.1 Orbital magnetic moments

Various important properties of magnetic materials, like magnetic anisotropies, magneto-optical effects, and for example magnetic dichroism in various types of electronic spectroscopies are caused by spin-orbit coupling. While spin magnetic moments for $3d$ transition metals and their alloys are described rather accurately by the LSDA, the orbital magnetic moments are typically underestimated. To improve the description of orbital magnetism the so-called orbital polarization correction (OP) scheme was introduced by Brooks *et al.* [79–81] as an additional *ad hoc* term added to the LSDA Hamiltonian. Later on it had been realized that the OP term can be systematically derived from current DFT [82]. Despite of a quite accurate description of the orbital moments for bulk systems, calculations based on the OP-term fails to predict the experimental values for impurities [83–85] and clusters on surfaces [86].

An alternative approach is based on the explicit account of local (on-site) many-body correlations. In particular, Solovyev *et al.* [87, 88] have shown by calculations based on the random-phase approximation that the OP-picture is one of the limits of the more general LSDA+U concept [89]. On the other hand, the LSDA+U approach fails to give a proper description for the spectral properties of the $3d$ transition metals. Examples for these problems are found in the calculated bandwidths, the spin splitting, the energetics of the Ni satellite and in the absence of quasiparticle damping, etc. [58, 90]. On the other hand, the explicit account for local correlations within the LSDA+DMFT approach should improve the description of the orbital magnetic moments [54, 55] as well as of the spectral properties [24, 25, 48, 56, 91]. As an example LSDA+DMFT results for the ferromagnetic transition metals Fe, Co and Ni are shown in Fig. 2. It was found that the use of DMFT hardly

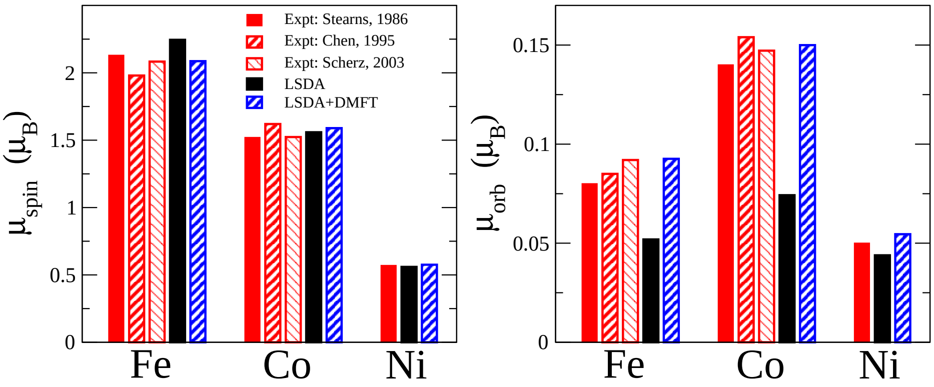

Figure 2: Spin (left panel) and orbital (right panel) magnetic moments in bcc Fe, hcp Co and fcc Ni calculated using LSDA+DMFT (hatched blue bars) compared with plain LSDA calculations (black filled bars) and experimental data (red bars).

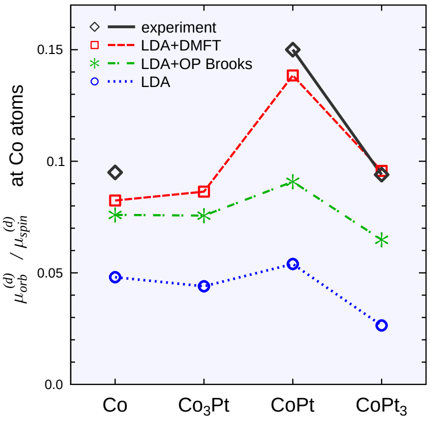

Figure 3: Ratios between the d components of μ_{orb} and μ_{spin} for Co in ordered CoPt obtained via various computational schemes compared with experiment [92].

changes the spin magnetic moments compared to plain LSDA-based calculations, that in turn give results already in very good agreement with experiment. Inclusion of the DMFT, on the other hand, increases the orbital moment and brings the theoretical values in very satisfying agreement with experiments. Concerning this a very important issue is the treatment of the double-counting term. A direct comparison of the calculated orbital magnetic moments with the corresponding experimental data clearly show that the AMF setting is most adequate for metallic transition metal systems. By construction the dynamical part of the self-energy Σ^{DMFT} behaves in the vicinity of the Fermi level as for a Fermi liquid. Therefore Σ^{DMFT} cannot noticeably affect integral quantities like spin and orbital magnetic moments. On the other hand, the applied AMF static double counting which splits the different orbitals only slightly at the Fermi level, has no impact on the renormalization of the density of states. As already mentioned, the application of the OP term for diluted magnetic moment systems is not much successful. Because the LSAD+DMFT method leads to more accurate results in this case, we performed LSDA+DMFT calculations for various CoPt ordered phases [55]. In Fig. 3 we show the *ratios* between the orbital and spin magnetic moments, which can be deduced from x-ray magnetic circular dichroism (XMCD) measurements. It follows from Fig. 3 that the LSDA systematically underestimates $\mu_{\text{orb}}^{(d)}/\mu_{\text{spin}}^{(d)}$ for Co in various

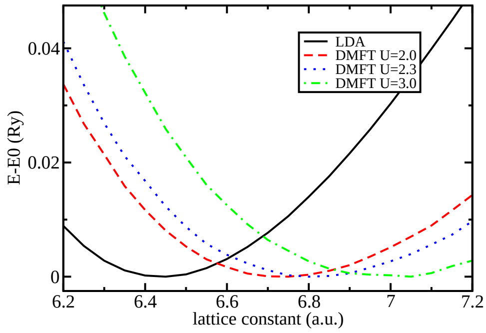

		EXP	LSDA	$U = 2.0$ eV
V_0(a.u.^{3})	FP-LMTO	73.52	67.88	76.20
	KKR		66.86	76.28
B(GPa)	FP-LMTO	186	260	163
	KKR		280	171

Figure 4: Left: Total energy of Ni calculated by means of the LSDA and LSDA+DMFT as a function of the lattice parameter a for various values of the parameter U. Right: Computed values of the equilibrium atomic volume V_0 and the bulk modulus B for the the standard LSDA-DFT method and for the LSDA+DMFT scheme in comparison with experiment [31].

compounds. This deficiency increases with increasing Pt content: the experimental $\mu^{(d)}_{\text{orb}}/\mu^{(d)}_{\text{spin}}$ ratio exceeds the LSDA result twice for bulk Co, three times for CoPt and four times for CoPt$_3$. Employing the OP scheme of Brooks increases the $\mu^{(d)}_{\text{orb}}/\mu^{(d)}_{\text{spin}}$ ratio and partially compensates for the deficiency of the LSDA. This compensation is nearly complete for bulk Co but it becomes insufficient as the Pt content increases. Employing the LSDA+DMFT, on the other hand, leads to a nearly perfect reproduction of the experimental $\mu^{(d)}_{\text{orb}}/\mu^{(d)}_{\text{spin}}$ ratio at Co atoms for bulk Co, CoPt, as well as CoPt$_3$.

3.1.2 Total energy calculations

As already mentioned, most of the LSDA+DMFT applications up to now are connected with spectral function calculations and related properties. However the predictive power of any LSDA+DMFT approach can be achieved only by an accurate description of the total energies and related phenomena like forces or lattice relaxations. A step towards investigations on the equilibrium structure of correlated systems, which are based on total energy calculations in the framework of the full potential KKR implementation of the LSDA+DMFT method, is found in [31]. Results obtained for ferromagnetic Ni are presented in Fig. 4. It is well known that in the framework of LSDA the equilibrium value of the lattice constant is slightly underestimated (typically by 3%) with respect to the experimental value. Concerning the calculations based on the LSDA+DMFT, one notices that the results are strongly dependent on the value of the Hubbard U. The best results are obtained for $U = 3$eV, i.e. for a value which is smaller as commonly accepted. This discrepancy can be assigned to the perturbative nature of the SPTF solver [31, 57]. However, for $U = 3$eV we obtained a reasonable agreement also for the bulk modulus. In the case of Ni a satisfying result can also be obtained by using gradient corrected functionals (GGA) [5]. On the other hand, in the case of γ-Mn which is considered to be a material on the border between moderate and strong correlations [59, 93] the change of the exchange correlation potential from LSDA to GGA does not solve all the problems and it remains a significant difference between theory and experiment. The atomic volume is underestimated and the anomalously low value of the bulk modulus ($B = 90 - 130$GPa [94, 95]) is strongly overestimated by LSDA. This problem can be solved by

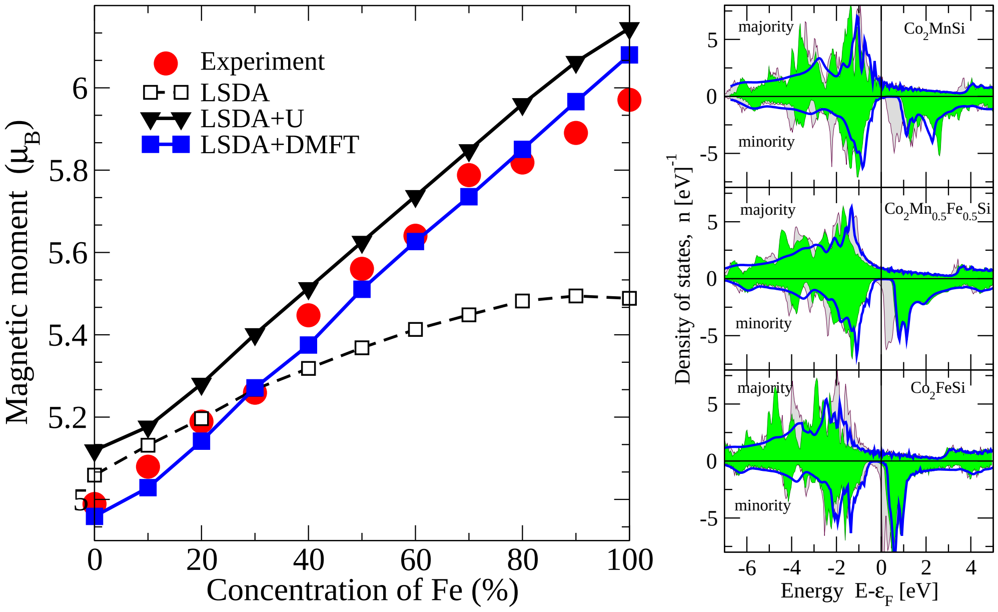

Figure 5: Left: Comparison of the total magnetic moments for $Co_2Mn_xFe_{1-x}Si$ compounds calculated within LSDA (black dashed line, opened squares), LSDA+U (black triangles) and LSDA+DMFT (blue squares) with the results of the SQUID magnetic measurements (red circles) [98]. Right: The total spin-resolved DOS curves for Co_2MnSi, $Co_2Mn_{0.5}Fe_{0.5}Si$ and Co_2FeSi calculated within LSDA (light/grey filled area), LSDA+U (dark/green filled area) and LSDA+DMFT (blue line). ($U_{\mathrm{Co,Mn,Fe}} = 3.0$eV and $J_{\mathrm{Co,Mn,Fe}} = 0.9$eV)

the LSDA+DMFT [31]. Interestingly a combination of the GGA and the DMFT in general leads only to moderately changes compared to plain GGA results, therefore demonstrates the general applicability of the LSDA+DMFT.

3.1.3 LSDA+DMFT for disordered alloys

Representing the electronic structure in terms of the Green's function allows for a straightforward combination of the LSDA+DMFT method with the CPA alloy theory, as both schemes are used up to now on a single site-level. This combined approach was applied to study the magnetic properties of a number of disordered substitutional transition metal alloys [16, 54, 56, 96]. An interesting class of materials for magneto-electronic applications is found in the family of half-metallic Heusler ferromagnets [97]. These materials show, for example, interesting properties connected with correlation effects, like as for example so called non-quasi particle states [23]. Special attention had been paid to Co_2MnSi, Co_2FeSi and to the substitutional series $Co_2Mn_xFe_{1-x}Si$ of Heusler half-metals which show a large minority band gap (of about 0.4eV) and a very high Curie temperature of about 1000K [98]. In Fig. 5 we present the total magnetic moments of the substitutional disordered alloy $Co_2Mn_xFe_{1-x}Si$. Our calculations show a monotonous increase with Fe content in the magnetic moment in analogy to the Slater-Pauling curve within the whole range of Fe concentrations. It turned out that the static treatment of correlation effects (on the level of LSDA+U) is important for a reliable description of the minority band gap [99] for this class of materials. The additional dynamical effect appearing within LSDA+DMFT only slightly reduces the spin magnetic moment.

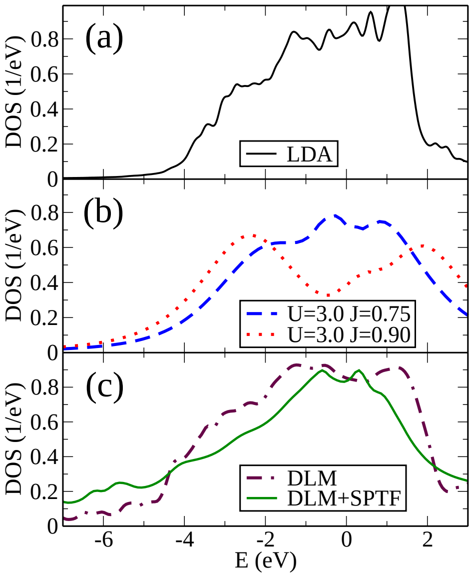

Figure 6: Comparison of the density of states of the $3d$ electrons in γ-Mn obtained by different approaches: (a) DFT-LDA (b) QMC with $U = 3.0$eV and different values of J. (c) DLM and DLM+SPTF for $U = 3.0$eV and $J = 0.8$eV.

The dynamical correlations appear to be more significant for the spectroscopic properties. As it follows from the right panel of Fig. 5, the LSDA+U enlarges the minority spin gap. Adding the DMFT causes a shift of the d-states towards the Fermi level and a substantial broadening of the DOS within the range between -2 and -8eV is observed. This effect can be seen directly in the angle-integrated valence band photoemission spectra [96].

Another interesting application of the CPA is to deal with thermal fluctuations of magnetic moments by use of the so called disordered local moment model (see Sec. 2.2.2). Its combination with the DMFT was recently demonstrated by a corresponding application to γ-Mn [59]. Here, it turned out that instead of the cumbersome and computationally expensive QMC calculations, the proposed combination of SPTF and the DLM approach can be used to describe adequately the high temperature properties of γ-Mn. In Fig. 6 a comparison of the densities of states of $3d$ electrons in γ-Mn obtained by different computational schemes is presented. The upper panel (a) and the middle panel (b) display the bare LDA results and the LDA+DMFT results with the QMC solver for $U = 3\,\mathrm{eV}$ and $J = 0.75\,\mathrm{eV}$ or $J = 0.9\,\mathrm{eV}$. In the lower panel (c) the density of states obtained within the DLM approach is reported, both for LSDA and LSDA+DMFT by use of the SPTF solver ("DLM+SPTF"). As the bare DLM describes the fluctuations in a very simple way, only a weak indication of three peak structures is observed. However the width of the $3d$-band is too large, since it derives from the single particle LDA density of states. On the other hand, in DLM+SPTF we can properly describe the shrinking of the $3d$ band, as already observed for Fe, Co and Ni [25, 58]. In comparison with the QMC calculations, the peak around $-2\,\mathrm{eV}$ is less pronounced. This is due to the perturbative nature of SPTF, which tends to shift the correlation effects related to the formation of non-coherent satellites. For example, the famous $-6\,\mathrm{eV}$ satellite of Ni is found at about $-8\,\mathrm{eV}$ [24]. In the case of γ-Mn the spectral weight is transferred to the region between -4 and $-6\,\mathrm{eV}$. In conclusion, it seems that the DLM+SPTF can reproduce QMC results for the moderately correlated regime. But, as it is shown in panel

(b) of Fig. 6 only a slight change of the parameter J (from 0.75 to 0.9eV) drives the γ-Mn into the strong correlation regime. This is because of the appearance of the Hubbard band. In fact, this tendency also strongly changes the temperature dependence of the magnetic moment. For the smaller value of J (moderately correlated system) spin fluctuations are reduced because of the presence of strong orbital fluctuations. For the higher value of J (strongly correlated limit) a strong fluctuating local moment is formed. This transition happens close to the physical value of Hund's exchange J. These different tendencies had been studied before in the two-orbital Hubbard model [100], but it is interesting to see that they can be quantitatively described in a real material with five orbitals and realistic hybridizations.

3.2 LSDA+DMFT for calculations of spectroscopic properties

3.2.1 Angle-integrated valence band photoemission: Fano effect

Spin-orbit coupling gives rise to many interesting phenomena in the electron spectroscopy of magnetic solids. A rather straightforward access to the understanding of these phenomena is provided by the study of the Fano effect. This effect was predicted by Fano at the end of the sixties and denotes the fact that one obtains a spin-polarized photoelectron current even for non-magnetic systems if the excitation is done using circularly polarized light [101]. At which, for non-magnetic samples the spin polarization of the photocurrent is reversed, this symmetry is in general broken for magnetically ordered systems leading to magnetic circular dichroism. However, in the case of magnetic materials, the spin polarization is usually due to the interplay between spin-orbit coupling and exchange splitting. Recently, we demonstrated by investigations on Fe, Co and Ni that the pure Fano effect can also be observed in angle-integrated valence band XPS (VB-XPS) for ferromagnets if circularly polarized light impinges perpendicular to the magnetization direction and if a subsequent spin analysis is done with respect to the direction of the photon beam [24]. This is demonstrated in Fig. 7 where the VB-XPS of the Fe, Co and Ni at a photon energy of 600eV is shown. The photon energy of 600eV has been used in order to increase the bulk sensitivity of the photoemission process. In the upper panel of Fig. 7 we compare experimental data with corresponding LSDA and LSDA+DMFT VB-XPS data based on the one-step model of photoemission. In all three cases the LSDA+DMFT considerably improves the agreement with the experiment. In particular, in the case of Ni LSDA+DMFT leads to the shrinking of the d-band width. In addition, use of the LSDA+DMFT scheme leads to a pronounced increase of the intensity in the regime of the 6eV satellite. For the total intensity of the Fe and Co signal we observed an pronounced improvement in the energy region from -2 to -8eV. A decomposition of the theoretical spectrum according to the angular momentum character of the initial state shows that the d-contribution is far dominating and that the spectrum essentially maps the corresponding DOS. This, in some sense, supports the common practice of comparing experimental XPS directly with the DOS. In the lower panel of Fig. 7 the corresponding spin difference $\Delta I^{+} = I^{+}_{\uparrow} - I^{+}_{\downarrow}$ (i.e. the difference of the currents of photoelectrons with spin-up and spin-down electrons, for excitation with left circularly polarized radiation) is shown. The occurrence of this spin current is a pure matrix element effect induced by spin-orbit coupling. In fact, one finds that the shape of the ΔI^{+} curves are very similar to those that can be found for non-magnetic Nobel metals [102, 103]. In fact, the amplitudes scale with the spin-orbit coupling parameter of the Fe, Co and Ni d-states. To achieve this rather good

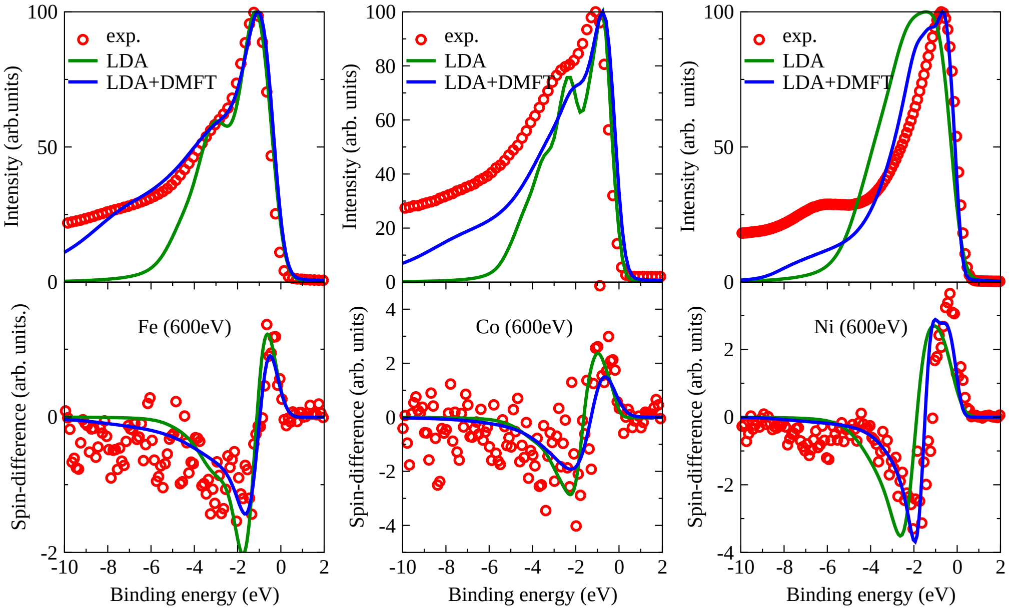

Figure 7: Top panel: The experimental (dots), LSDA (green line) and LSDA+DMFT (blue line) angle integrated valence band XPS spectra of bcc Fe, hcp Co and fcc Ni for a photon energy of 600eV . Lower panel: Spin difference $\Delta I^+ = I^+_\uparrow - I^+_\downarrow$ of the photocurrent for excitation with left circularly polarized light.

agreement with the experimental data for the ΔI^+ intensity distribution the fully self consistent LSDA+DMFT approach is obviously needed.

3.2.2 Angle-resolved photoemission within one-step model

In the previous Sec. 3.2.1 we showed angle-integrated XPS spectra which can be directly compared to the DOS ignoring matrix element effects. However, the most complete description of the band structure of correlated materials can be obtained by spin- and angle-resolved valence band photoemission. In the following section we present various examples of angle-resolved photoemission calculations done within the one-step model. These examples clearly demonstrate the need for such calculations in order to obtain a quantitative understanding of the corresponding experimental data.

The following examples concern the ferromagnetic transition metal systems Ni and Fe as prototype materials to study electronic correlations and magnetism beyond the LSDA scheme. In Fig. 8 we present a comparison between experimental photoemission data [64] and calculated spectra using different theoretical approaches [25]. In the upper row spin-integrated ARPES measurements from Ni(011) along $\overline{\Gamma Y}$ for different angles of emission are shown. The dotted lines represent the experimental data, whereas the solid lines denote the single-particle approach to the measured spectral function. Obviously, the LSDA-based calculation completely fails to describe the experimental data. The energetic positions of the theoretical peaks deviate strongly from the measured ones. Furthermore, the complicated intensity distributions that appear for higher emission angles are not accounted for by the LSDA-based calculations. In contrast, the non self consistent quasi-particle 3BS calculation provides a significant improvement when compared to the measured spectra. For

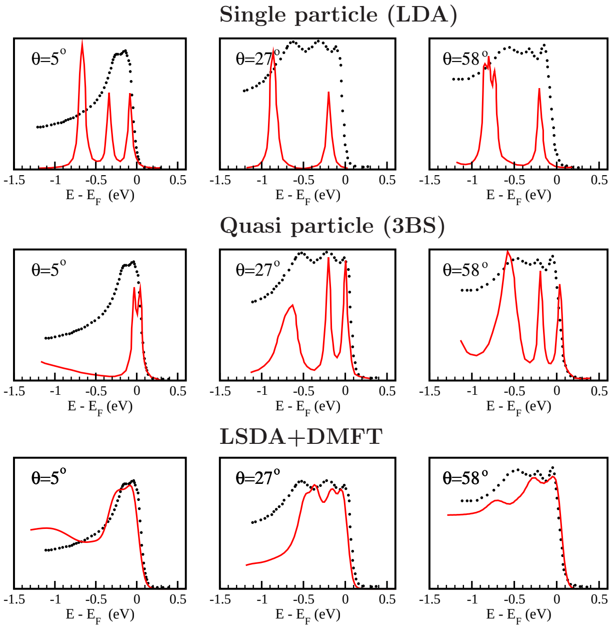

Figure 8: Spin-integrated ARPES spectra from Ni(011) along $\overline{\Gamma}Y$ for three different angles of emission. Upper row: comparison between LSDA-based calculation and experiment [64]; middle row: comparison between experiment and non self consistent quasi-particle calculations neglecting matrix element and surface effects [64]; lower row: spin-integrated LSDA+DMFT spectra including photoemission matrix elements (this work). Theory: solid red line, experiment: black dots.

the complete range of emission angles the energetic peak positions coincidence with the experiment within about 0.1 eV. Only the overall shape of the measured spectral intensities deviate from the calculations because of the neglect of multiple scattering and surface-related as well as matrix-element effects. In the experiment the various peaks seem to be more broadened and the spectral weight especially for nearly normal emission is shifted by about 0.1 eV to higher binding energies. In addition it seems that for very high emission angles like 60° an even more complicated peak structure is hidden due to limited experimental resolution. An additional spin-analysis is therefore highly desirable for these experiments.

Within our work we could go far beyond previous theoretical studies by combining a sophisticated many-body approach as the self consistent LSDA+DMFT method with the one-step based calculation of the corresponding spectral function. The self-energy within the DMFT has been applied only for d-states and can be calculated in terms of two parameters - the averaged screened Coulomb interaction U and the exchange interaction J. The screening of the exchange interaction is usually small and the value of J can be calculated directly and is approximately equal to 0.9 eV for all $3d$ elements. This value has been adopted for all our calculations presented here. For U we used a value of 3 eV. However, our test calculations showed that a somewhat different choice of U does not substantially changes the various features and trends in the calculated spectra. The intensity distributions resulting from the corresponding photoemission calculation are shown in the lower row of Fig. 8. A first inspection reveals very satisfying quantitative agreement between experiment and theory for all emission angles. Let us concentrate first on the excitation spectrum calculated for the emission angle $\Theta = 5°$. The spin-integrated spectrum exhibits a pronounced double-peak structure with binding energies of 0.1 eV and 0.3 eV. The second peak is slightly reduced in intensity

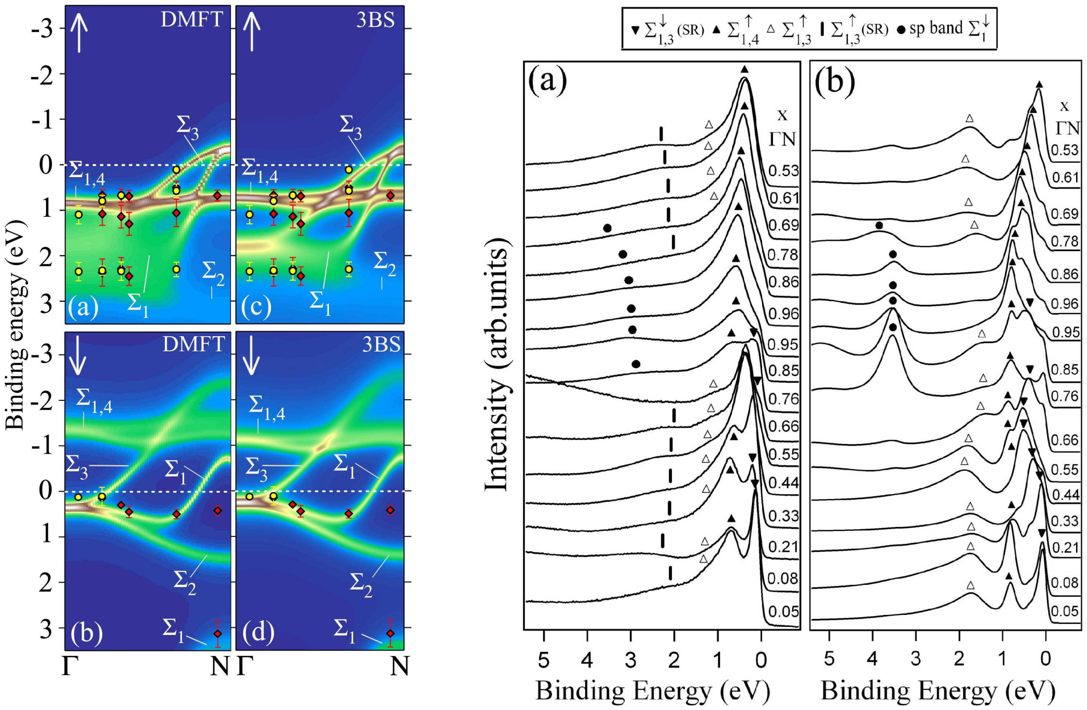

Figure 9: Left panel: Spin resolved Bloch spectral functions calculated within LSDA+DMFT and 3BS formalism . Corresponding experimental data points have been deduced from the normal emission spectra along the ΓN direction. Right panel: (a) Experimental spin-integrated photoemission spectra of the Fe(110) surface measured with p-polarization in normal emission along the ΓN direction of the bulk Brillouin zone. The curves are labeled by the wave vectors in units of ΓN=1.55 $\AA^{-1}$. (b) Corresponding one-step model calculations based on the LSDA+DMFT method which include correlations, matrix elements and surface effects.

which is also in accordance with the experimental findings. Furthermore, the width of the spectral distribution is quantitatively reproduced. The calculated binding energies are related to the real part of the self-energy that corrects the peak positions due to a dynamical renormalization of the quasiparticles which is missing in a typical LSDA-based calculation. The relative intensities of the different peaks, on the other hand, must be attributed to the matrix-element effects which enter our calculations from the very beginning via the one-step model of photoemission. The double-peak structure originates from excitation of the spin-split d-bands in combination with a significant amount of surface-state emission [104]. The two spectra calculated for high emission angles show the more broadened spectral distributions observed in experiment. An explanation can be given in terms of matrix-element effects, due to the dominating dipole selection rules. The spin-resolved spectra reveal a variety of d-band excitations in both spin channels, which in consequence lead to the complicated shape of the spectral distributions hardly to be identified in the spin-integrated mode.

The second example within this section concerns a spectroscopic study of ferromagnetic Fe [48]. In the left panel of Fig. 9 we compare the experimental peak positions from bulk like transitions with spin-resolved LSDA+DMFT spectral functions. In addition to these investigations we accounted for correlation effects within the 3BS approach [12]. Within the 3BS approach the self-energy is calculated using a configuration interaction-like expansion. In particular three-particle configurations like one hole plus one electron-hole pair are explicitly taken into account within 3BS-based calculations. The corresponding output can be directly related to the photoemission process and allows for a detailed analysis of various contributions to the self-energy (e.g., electron-hole lifetime). A more detailed quantitative comparison is shown in right panel of Fig. 9. Here we display a comparison between spin-integrated ARPES data and theoretical LSDA+DMFT based one-step photoemission calculations of Fe(110) along the ΓN direction of the bulk Brillouin zone (BZ) with p-polarized radiation. In our LSDA+DMFT investigation underlying the ARPES calculations we use for the averaged on-site Coulomb interaction U a value U=1.5 eV which lies between the experimental value U ≈1 eV [105] and a value U ≈2 eV obtained from theoretical studies [36, 54]. The k values associated with the spectra were calculated from the used photon energies ranging from 25 to 100 eV. Near the Γ point (k∼0.06 ΓN), the intense peak close to the Fermi level corresponds to a $\Sigma^{\downarrow}_{1,3}$ minority surface resonance, as indicated on top of Fig. 9. Experimentally, its $\Sigma^{\downarrow}_{3}$ bulk component crosses the Fermi level at k ∼0.33 ΓN, leading to a reversal of the measured spin-polarization and to a strong reduction of the intensity at k =0.68 ΓN in the minority channel. The peak at the binding energy BE∼0.7 eV, visible mainly for p-polarization in a large range of wave vectors between Γ and N, can be assigned to almost degenerate $\Sigma^{\uparrow}_{1,4}$ bulk-like majority states. A $\Sigma^{\uparrow}_{3}$ feature at BE∼1.1 eV dominates the spectrum close to the Γ-point. Depending on the polarization the degenerate $\Sigma^{\uparrow}_{1}$ states form a shoulder around the same BE. The broad feature around 2.2 eV, visible at various k-points, but not at the N-point, is related to a majority $\Sigma^{\uparrow}_{1,3}$ surface state. Around the N-point (0.76≤ k ≤1.0) and at BE≥3 eV we observe a $\Sigma^{\downarrow}_{1}$ band having strong sp character. The pronounced difference between its theoretical and experimental intensity distributions can be attributed to the fact that in the present calculations only the local Coulomb repulsion between d electrons is considered, without additional lifetime effects for the sp bands. Finally, we notice that the background intensity of the spectrum at k=0.66 ΓN, corresponding to a photon energy of 55 eV, is strongly increased due to the appearance of the Fe 3p resonance. The direct comparison of the calculated and experimental spectra turned out to be a very stringent check of Coulomb parameter U used in the calculations. This also applies to the DMFT self-energy, that was compared to its counterpart deduced from the experimental band dispersion and line width.

In conclusion, we have presented spectral function calculations of ferromagnetic Ni and Fe, which coherently combine an improved description of electronic correlations, multiple-scattering, surface emission, dipole selection rules and other matrix-element related effects that lead to a modification of the relative photoemission intensities. A similar study has been recently performed for Co(0001) [49]. This approach allows on the one hand side a detailed and reliable interpretation of high-resolution angle-resolved photoemission spectra of 3d-ferromagnets. On the other hand, it also allows for a very stringent test of new developments in the field of DMFT and similar many-body techniques.

3.2.3 One-step model of photoemission of disordered Ni$_x$Pd$_{1-x}$(001) alloy

In this section alloying effects in combination with electronic correlations are considered [56]. Fig. 10 shows a series of spectra of Ni$_x$Pd$_{1-x}$ as a function of the concentration x calculated for a

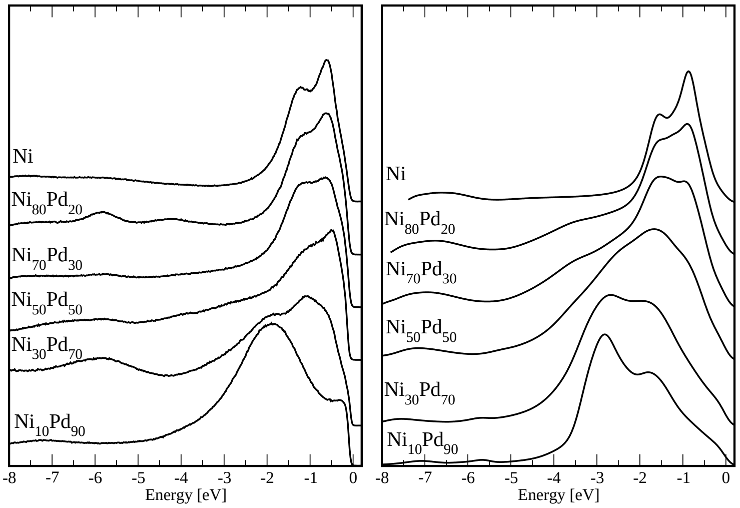

Figure 10: ARPES spectra taken from the $\mathrm{Ni}_x\mathrm{Pd}_{1-x}(001)$ alloy surfaces as a function of the concentration x for a fixed photon energy of $h\nu$=40.0 eV along ΓX in normal emission. Experimental data shown in the left panel calculated spectra presented in the right panel. Depending on the concentration x a pronounced shift in spectral weight towards the Fermi level is visible.

photon energy $h\nu$=40 eV with linear polarized light. The experimental data are shown in the left panel and the corresponding LSDA+DMFT-based photoemission calculations are presented in the right one. Our theoretical analysis shows that starting from the pure Ni, the agreement is fully quantitative with deviations less than 0.1 eV binding energy, as expected. Going to the $\mathrm{Ni}_{0.80}\mathrm{Pd}_{0.20}$ alloy the agreement is comparable good for binding energies between the Fermi energy and 2 eV. Inspecting the density of states (DOS) for the $\mathrm{Ni}_{0.80}\mathrm{Pd}_{0.20}$ alloy this fact becomes explainable, because this energy interval represents the Ni-dominated region. The Pd derived states start to appear at about 2 eV below E_F besides of the small dip at the Fermi level. For higher binding energies the agreement is also very good, although a bit more structure is observable in the theory, especially around 3.5 eV. An explanation for this behavior can be found in terms of lifetime effects, but it should be mentioned here that background in the experimental spectra due to secondary electrons was not considered in the theoretical analysis. From the $\mathrm{Ni}_{0.70}\mathrm{Pd}_{0.30}$ alloy system it becomes clearly visible that the deviation between theory and experiment is mainly introduced for increasing concentration of Pd. This can be seen from the spectra for $\mathrm{Ni}_{0.50}\mathrm{Pd}_{0.50}$ and $\mathrm{Ni}_{0.30}\mathrm{Pd}_{0.70}$ alloys shown next in the series. In addition, the spectra of $\mathrm{Ni}_{0.30}\mathrm{Pd}_{0.70}$ reveal some deviations near the Fermi level. Also, the spectral intensity of the Ni surface resonance, that appears at about 0.5 eV binding energy is underestimated in the calculation when compared to the experiment.

Our spectroscopic analysis has clearly demonstrated that the electronic properties of the $\mathrm{Ni}_x\mathrm{Pd}_{1-x}$ alloy system depend very sensitively on the interplay of alloying and electronic correlation. A description within the LSDA approach in combination with the CPA results in a quantitative description of the electronic structure of $\mathrm{Ni}_x\mathrm{Pd}_{1-x}$ [56]. This example may illustrate that the use of the CPA alloy theory self consistently combined with LSDA+DMFT approach serves as a powerful tool for electronic structure calculations, whereas the application of the fully relativistic one-step model of photoemission, which takes into account chemical disorder and electronic correlation on equal footing guarantees a quantitative analysis of the corresponding spectroscopic data.

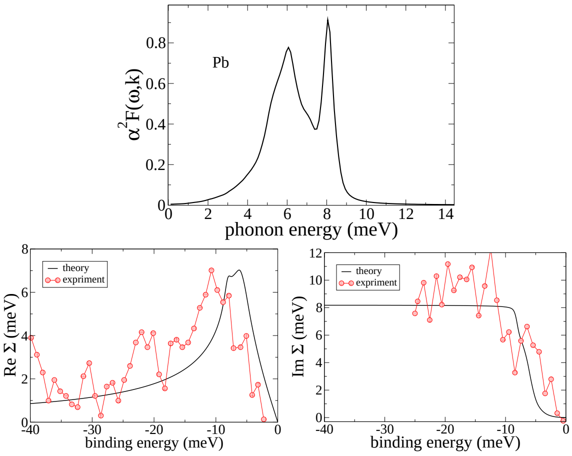

Figure 11: Upper panel: Calculated Eliashberg function $\alpha^2 F_k(\omega)$ for Pb(110) for $\mathbf{k} = \frac{\pi}{a}(0.17, 1., 0.17)$. Lower panel: corresponding k-dependent self-energy, real part shown on left, imaginary part shown on the right.

3.3 Effects of electron-phonon interaction in angle-resolved photoemission

In the following section we want to demonstrate that the formalism presented in Sec. 2.2 can be extended in order to include a $\vec{k}$-dependent self-energy. In detail, we discuss the effect of electron-phonon coupling on the angle-resolved photoemission of Pb(110).

Nowadays, high resolution photoemission measurements allow to investigate in great detail the electronic structure of materials close to the Fermi level. This gives access to energy bands modified by electron-phonon interaction, and therefore serves as a very important spectroscopic tool to characterize transport properties or, for example, properties of super-conducting materials [106–109]. Modifications of the electronic structure generated by electron-phonon interaction are typically not accounted for in LSDA-based band-structure calculations. The theoretical treatment of electron-phonon effects requires the use of many-body techniques which originally had been developed to give a quantitative description of strong electronic correlation effects. The self-energy approach often applied in many-body calculations can be used as well to represent the electron-phonon interaction. Accordingly, having the electronic structure obtained by an ab-initio calculation, the modifications due to electron-phonon interaction can be described via an electron-phonon self-energy $\Sigma(\mathbf{k}, E_k)$ [110, 111]. The electron-phonon self-energy is derived using many-body perturbation theory within second order and is expressed in terms of the momentum-resolved Eliashberg function $\alpha^2 F_k(\omega)$. To obtain explicitly the electron-phonon self-energy, we focus our attention on the Eliashberg function as the main quantity determined by all coupled electronic and phononic states of the system. This function can efficiently be reformulated in terms of the Green's function [112, 113] and accordingly by calculated directly using KKR formalism. For this propose the phonon dispersions and corresponding matrix elements have been calculated within the real space KKR formulation of the rigid sphere approximation.

The complex self-energy in general consists of contributions due to electron-electron and electron-impurity scattering, as well as due to electron-phonon scattering (Σ_{el-ph}). The real part of Σ_{el-ph} is responsible for band renormalization around E_{F}. On the other hand the imaginary part part of

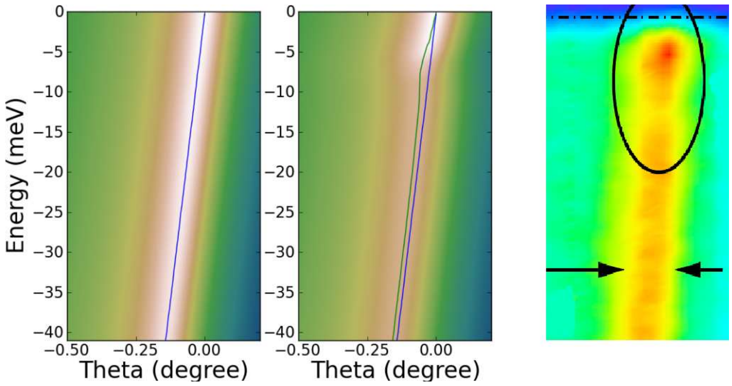

Figure 12: ARPES spectra taken from the Pb(110) surface excluding (left panel) and including (middle panel) phonons via a corresponding electron-phonon self-energy Σ_{el-ph}. Corresponding experimental data are shown on the right panel [115].

Σ_{el-ph} describes lifetime effects. These quantities are determined by electron-phonon scattering induced quasiparticle lifetimes, measurable in photoemission experiments. To demonstrate the effect of electron-phonon interactions on the electronic quasi-particle states near E_{F} we present photoemission calculations for Pb, which serves as a prototype system and compare our theoretical results to corresponding experimental data [114]. Pb is of special interest because of the presence of strong electron-phonon interactions which in particular lead to the superconducting state at low temperatures [106, 109].

The calculations have been performed for energies close to the Fermi level. The wave vectors in the BZ ($\mathbf{k} = \frac{\pi}{a}(0.17, 1., 0.17)$) correspond to the experimental geometry [109]. Fig. 11 shows a comparison between the experimental and theoretical real and imaginary parts of the self-energy Σ_k. Obviously, the agreement is very satisfying. In general, it is possible to deduce a phononic self-energy from measured photoemission spectra. The imaginary part of the self-energy can be estimated from the full width at half maximum of the energy distribution curves fitted by a Lorentzian. The real part is then obtained by a Kramers-Kronnig transformation. However, in cases where for example several transitions appear close to the Fermi level or even additional surface contributions to the photocurrent take place, this analysis might be questionable. Therefore, it seems to be more reliable to make a direct comparison between angle-resolved photoemission calculations and corresponding experimental data. For this purpose we developed a scheme that allows to include directly a $\mathbf{k}$-dependent self-energy into the one-step model of photoemission. In Fig. 12 we present photoemission spectra calculated for the two cases without (left panel) and with (middle panel) electron-phonon interactions and compare them to the corresponding measurements [115]. The contour plot has been calculated for HeI radiation along $\bar{\Gamma}\bar{\mathrm{X}}$. More precisely, bands forming the locally tubular Fermi surface of Pb(110) crosses E$_F$ at about 5° off-normal emission along $\bar{\Gamma}\bar{\mathrm{X}}$. In the middle panel of Fig. 12 a clear renormalization of the bare band (often called *kink*) at 8meV binding energy is observable. This effect appears just where the real part of the self-energy reaches its maximum. Furthermore, an additional broadening of the spectral features due to the imaginary part of the phononic self-energy is visible in the calculated spectra. This, of course, completes a lifetime analysis of spectral features in a quantitative sense because the imaginary part of the phononic self-energy can be identified as the last contribution that has to be considered in addition to impurity scattering and electronic correlation related broadening mechanisms of photoemission intensities. As an outlook the above scheme can straightforwardly be extended to combine the electron-phonon interaction with LSDA+DMFT calculations. This will allow a electron-phonon interaction studies of the correlated materials like for example fcc-Ni [116].

4 Summary and concluding remarks

In summary, we have reviewed a LSDA+DMFT implementation within the KKR method. In particular this approach was chosen because the KKR method represents the electronic structure by the corresponding single-particle Green's function leading therefore to a number of very attractive features of the scheme. The fully-self consistent full-potential implementation turned out to be a very powerful tool to study ground state as well as spectroscopic properties of transition metals, alloys and their surfaces. The fully-relativistic formulation allows to study spin-orbit coupling induced properties as, e.g. orbital magnetic moments or magnetic dichroic phenomena in photoemission. The TMA and SPTF solver used so far clearly imposes a restriction to moderately correlated materials. To get access to strongly correlated systems the adaption of QMC based solvers to the KKR implementation is needed.

Of course, the LSDA+DMFT method in its standard form is not an *ab-initio* method mostly due to use of the Coulomb parameter U. Various schemes have been proposed to calculate U like the constrained random phase approximation or constrained LSDA. The scheme developed by Cococcioni et al. [36] seems to be especially attractive, as it might be applicable without modifications to surfaces and nano-structures within the embedding KKR technique by avoiding the super-cell approach. With reliable values for the Coulomb parameter U the KKR implementation of the LSDA+DMFT will open the way to investigate the impact of correlation effects on structural and volume dependent properties in a quantitative way. In particular systems with reduced dimensionality, like 2D surfaces or nano-structures deposited on surfaces can be straightforwardly calculated within the KKR implementation of LSDA+DMFT. Furthermore, as it has been demonstrated, a $\vec{k}$-dependent self-energy can be included into the KKR method. This allows to discuss non-local correlation effects, for example, on the basis of cluster DMFT.

All these developments can be directly tested by a direct comparison with the corresponding experiments like i.e. angle-resolved photoemission, magnetic Compton profiles or magneto optics. Finally, developments connected with resonant and time-dependent spectroscopy become more and more important to gain detailed insights into the physics of correlated materials.

5 Acknowledgments

It is a pleasure to acknowledge the collaboration with many colleagues on the various aspects occurring in this selective review: in particular J. Braun, S. Mankovskyy, D. Ködderitzsch and H. Ebert from Munich group supporting and helping to develop this project and A. Lichtenstein, M. Katsnelson, L. Chioncel, I. DiMarco, L. Pourovskii, S. Chadov and others for many discussions on the DMFT. As it is clear from this paper, many tight collaborations with various experimental groups stimulated the present work to a large extend, in particular with: N. Brooks, H. Dürr, J. Fink, J. Sanchez-Barriga, G. Fecher, C.M. Schneider, F. Matthes, F. Reinert and Ch. Fadley. Last but not least, financial support from German the funding agencies DFG and the ministry BMBF is acknowledged.

References

[1] R. M. Dreizler and E. K. U. Gross, *Density Functional Theory* (Springer-Verlag, Heidelberg, 1990).

[2] P. Hohenberg and W. Kohn, Phys. Rev. **136**, B 864 (1964).

[3] W. Kohn and L. J. Sham, Phys. Rev. **140**, A 1133 (1965).

[4] R. O. Jones and O. Gunnarsson, Rev. Mod. Phys. **61**, 689 (1989).

[5] J. P. Perdew, K. Burke, and M. Ernzerhof, Phys. Rev. Lett. **77**, 3865 (1996).

[6] J. D. Talman and W. F. Shadwick, Phys. Rev. A **14**, 36 (1976).

[7] E. Engel, in *Relativistic Electronic Structure Theory. Part I. Fundamentals*, Elsevier, edited by P. Schwerdtfeger (Amsterdam, 2002), pp. 523–621.

[8] J. P. Perdew and A. Zunger, Phys. Rev. B **23**, 5048 (1981).

[9] A. Georges, G. Kotliar, W. Krauth, and M. J. Rozenberg, Rev. Mod. Phys. **68**, 13 (1996).

[10] L. Hedin, Phys. Rev. **139**, A796 (1965).

[11] V. Anisimov, F. Aryasetiawan, and A. Lichtenstein, J. Phys.: Cond. Mat. **9**, 767 (1997).

[12] C. Calandra and F. Manghi, Phys. Rev. B **50**, 2061 (1994).

[13] G. Kotliar, S. Y. Savrasov, K. Haule, V. S. Oudovenko, O. Parcollet, and C. A. Marianetti, Rev. Mod. Phys. **78**, 865 (2006).

[14] K. Held, Adv. Phys. **56**, 829 (2007).

[15] R. C. Albers, N. E. Christensen, and A. Svane, J. Phys.: Condens. Matter **21**, 343201 (2009).

[16] J. Minár, L. Chioncel, A. Perlov, H. Ebert, M. I. Katsnelson, and A. I. Lichtenstein, Phys. Rev. B **72**, 45125 (2005).

[17] H. Ebert, S. Bornemann, J. Braun, D. Ködderitzsch, S. Lowitzer, S. Mankovskyy, J. Minár, M. Offenberger, S. Polesya, and V. Popescu, "Highlight of the Month" in: Newsletter of the Ψ_k Network **97**, 79 (2010).

[18] W. Metzner and D. Vollhardt, Phys. Rev. Lett. **62**, 324 (1989).

[19] V. I. Anisimov, A. I. Poteryaev, M. A. Korotin, A. O. Anokhin, and G. Kotliar, J. Phys.: Cond. Mat. **9**, 7359 (1997).

[20] M. Katsnelson and A. Lichtenstein, J. Phys.: Cond. Mat. **11**, 1037 (1999).

[21] K. Sato and H. Katayama-Yoshida, Hyperfine Interactions **no.3-4&137**, 737 (2001).

[22] S. Y. Savrasov and G. Kotliar, Phys. Rev. B **69**, 245101 (2004).

[23] M. I. Katsnelson, V. Y. Irkhin, L. Chioncel, A. I. Lichtenstein, and R. A. de Groot, Rev. Mod. Phys. **80**, 315 (2008).

[24] J. Minár, H. Ebert, C. De Nadaï, N. B. Brookes, F. Venturini, G. Ghiringhelli, L. Chioncel, M. I. Katsnelson, and A. I. Lichtenstein, Phys. Rev. Lett. **95**, 166401 (2005).

[25] J. Braun, J. Minár, H. Ebert, M. I. Katsnelson, and A. I. Lichtenstein, Phys. Rev. Lett. **97**, 227601 (2006).

[26] L. Chioncel, L. Vitos, I. A. Abrikosov, J. Kollár, M. I. Katsnelson, and A. I. Lichtenstein, Phys. Rev. B **67**, 235106 (2003).

[27] S. Y. Savrasov, G. Kotliar, and E. Abrahams, Nature **410**, 793 (2001).

[28] B. Amadon, S. Biermann, A. Georges, and F. Aryasetiawan, Phys. Rev. Lett. **96**, 066402 (2006).

[29] L. V. Pourovskii, B. Amadon, S. Biermann, and A. Georges, Phys. Rev. B **76**, 235101 (2007).

[30] J. Kunes, A. V. Lukoyanov, V. I. Anisimov, L. T. Scalettar, and W. E. Pickett, Nature Materials **7**, 198 (2008).

[31] I. Di Marco, J. Minár, S. Chadov, M. I. Katsnelson, H. Ebert, and A. I. Lichtenstein, Phys. Rev. B **79**, 115111 (2009).

[32] I. Leonov, D. Korotin, N. Binggeli, V. I. Anisimov, and D. Vollhardt, Phys. Rev. B **81**, 075109 (2010).

[33] V. I. Anisimov, D. E. Kondakov, A. V. Kozhevnikov, I. A. Nekrasov, Z. V. Pchelkina, J. W. Allen, S.-K. Mo, H.-D. Kim, P. Metcalf, S. Suga, A. Sekiyama, G. Keller, I. Leonov, X. Ren, and D. Vollhardt, Phys. Rev. B **71**, 125119 (2005).

[34] F. Lechermann, A. Georges, A. Poteryaev, S. Biermann, M. Posternak, A. Yamasaki, and O. K. Andersen, Phys. Rev. B **74**, 125120 (2006).

[35] O. K. Andersen and T. Saha-Dasgupta, Phys. Rev. B **62**, R16219 (2000).

[36] M. Cococcioni and S. de Gironcoli, Phys. Rev. B **71**, 035105 (2005).

[37] J. S. Faulkner and G. M. Stocks, Phys. Rev. B **21**, 3222 (1980).

[38] P. Strange, H. Ebert, J. B. Staunton, and B. L. Györffy, J. Phys.: Cond. Mat. **1**, 2959 (1989).

[39] A. H. MacDonald and S. H. Vosko, J. Phys. C: Solid State Phys. **12**, 2977 (1979).

[40] A. Gonis and W. H. Butler, *Multiple scattering in solids*, *Graduate Texts in Contemporary Physics* (Springer, Berlin, 1999).

[41] E. Tamura, Phys. Rev. B **45**, 3271 (1992).

[42] E. N. Economou, *Green's Functions in Quantum Physics* (Springer-Verlag, New York, 1990).

[43] R. Zeller, J. Deutz, and P. H. Dederichs, Solid State Commun. **44**, 993 (1982).

[44] K. Wildberger, P. Lang, R. Zeller, and P. H. Dederichs, Phys. Rev. B **52**, 11502 (1995).

[45] L. V. Pourovskii, M. I. Katsnelson, and A. I. Lichtenstein, Phys. Rev. B **72**, 115106 (2005).

[46] S. Chadov, Application of Many-Body Perturbation Theory to the Description of Correlated Metals, Doktorarbeit, Universität München, 2007.

[47] S. Biermann, F. Aryasetiawan, and A. Georges, Phys. Rev. Lett. **90**, 086402 (2003).

[48] J. Sánchez-Barriga, J. Fink, V. Boni, I. Di Marco, J. Braun, J. Minár, A. Varykhalov, O. Rader, V. Bellini, F. Manghi, H. Ebert, M. I. Katsnelson, A. I. Lichtenstein, O. Eriksson, W. Eberhardt, and H. A. Dürr, Phys. Rev. Lett. **103**, 267203 (2009).

[49] J. Sánchez-Barriga, J. Minár, J. Braun, A. Varykhalov, V. Boni, I. Di Marco, O. Rader, V. Bellini, F. Manghi, H. Ebert, M. I. Katsnelson, A. I. Lichtenstein, O. Eriksson, W. Eberhardt, H. A. Dürr, and J. Fink, Phys. Rev. B **82**, 104414 (2010).

[50] P. Soven, Phys. Rev. **156**, 809 (1967).

[51] J. S. Faulkner, Prog. Mater. Sci. **27**, 3 (1982).

[52] V. Drchal, V. Janiš, and J. Kudrnovský, Phys. Rev. B **60**, 15664 (1999).

[53] I. Turek, V. Drchal, J. Kudrnovský, M. ˇ Sob, and P. Weinberger, *Electronic structure of disordered alloys, surfaces and interfaces* (Kluwer Academic Publ., Boston, 1997).

[54] S. Chadov, J. Minár, M. I. Katsnelson, H. Ebert, D. Ködderitzsch, and A. I. Lichtenstein, Europhys. Lett. **82**, 37001 (2008).

[55] O. Šipr, J. Minár, S. Mankovsky, and H. Ebert, Phys. Rev. B **78**, 144403 (2008).

[56] J. Braun, J. Minár, F. Matthes, C. M. Schneider, and H. Ebert, Phys. Rev. B **82**, 024411 (2010).

[57] M. I. Katsnelson and A. I. Lichtenstein, European Physics Journal B **30**, 9 (2002).

[58] A. Grechnev, I. Di Marco, M. I. Katsnelson, A. I. Lichtenstein, J. Wills, and O. Eriksson, Phys. Rev. B **76**, 035107 (2007).

[59] I. D. Marco, J. Minár, J. Braun, M. I. Katsnelson, A. Grechnev, H. Ebert, A. I. Lichtenstein, and O. Eriksson, Eur. Phys. J. B **72**, 473 (2009).

[60] B. L. Gyorffy, A. J. Pindor, J. Staunton, G. M. Stocks, and H. Winter, J. Phys. F: Met. Phys. **15**, 1337 (1985).

[61] J. Staunton, Rep. Prog. Phys. **57**, 1289 (1994).

[62] A. M. N. Niklasson, J. M. Wills, M. I. Katsnelson, I. A. Abrikosov, O. Eriksson, and B. Johansson, Phys. Rev. B **67**, 235105 (2003).

[63] K. Held, I. A. Nekrasov, G. Keller, V. Eyert, N. Blümer, A. K. McMahan, R. T. Scalettar, T. Pruschke, V. I. Anisimov, and D. Vollhardt, phys. stat. sol. (b) **243**, 2599 (2006).

[64] F. Manghi, V. Bellini, J. Osterwalder, T. J. Kreutz, P. Aebi, and C. Arcangeli, Phys. Rev. B **59**, R10409 (1999).

[65] J. Braun, Rep. Prog. Phys. **59**, 1267 (1996).

[66] J. B. Pendry, *Low energy electron diffraction* (Academic Press, London, 1974).

[67] J. B. Pendry, Surf. Sci. **57**, 679 (1976).

[68] J. F. L. Hopkinson, J. B. Pendry, and D. J. Titterington, Comp. Phys. Commun. **19**, 69 (1980).

[69] C. N. Berglund and W. E. Spicer, Phys. Rev. **136**, A1030 (1964).

[70] K. Kambe, Z. Naturf. **22a**, 322 (1967).

[71] J. M. MacLaren, S. Crampin, D. D. Vvedensky, and J. B. Pendry, Phys. Rev. B **40**, 12164 (1989).

[72] G. Malmström and J. Rundgren, Comp. Phys. Commun. **19**, 263 (1980).

[73] G. Borstel, Appl. Physics A **38**, 193 (1985).

[74] C. Caroli, D. Lederer-Rozenblatt, B. Roulet, and D. Saint-James, Phys. Rev. B **8**, 4552 (1973).

[75] J. Braun, in *New developments in UP- and XP-spectroscopy from ferromagnetic materials, in Band-Ferromagnetism*, *Lecture Notes in Physics*, edited by K. Baberschke and et al (Springer Verlag, Berlin, 2001), p. 341.

[76] G. Hilgers, M. Potthoff, N. Müller, U. Heinzmann, L. Haunert, J. Braun, and G. Borstel, Phys. Rev. B **52**, 14859 (1995).

[77] P. J. Durham, J. Phys. F: Met. Phys. **11**, 2475 (1981).

[78] B. Ginatempo, P. J. Durham, and B. I. Györffy, J. Phys.: Cond. Mat. **1**, 6483 (1989).

[79] M. S. S. Brooks, Physica B **130**, 6 (1985).

[80] O. Eriksson, B. Johansson, and M. S. S. Brooks, J. Phys.: Cond. Mat. **1**, 4005 (1989).

[81] O. Eriksson, M. S. S. Brooks, and B. Johansson, Phys. Rev. B **41**, 7311 (1990).

[82] H. Eschrig, M. Sargolzaei, K. Koepernik, and M. Richter, Europhys. Lett. **72**, 611 (2005).

[83] W. D. Brewer, A. Scherz, C. Sorg, H. Wende, K. Baberschke, P. Bencok, and S. Frota-Pessôa, Phys. Rev. Lett. **93**, 077205 (2004).

[84] S. Frota-Pessôa, Phys. Rev. B **69**, 104401 (2004).

[85] M. Sargolzaei, Ph.D. thesis, Fakultät Mathematik und Naturwissenschaften der Technischen Universität Dresden, 2006.

[86] P. Gambardella, S. Rusponi, M. Veronese, S. S. Dhesi, C. Grazioli, A. Dallmeyer, I. Cabria, R. Zeller, P. H. Dederichs, K. Kern, C. Carbone, and H. Brune, Science **300**, 1130 (2003).

[87] I. V. Solovyev, A. I. Liechtenstein, and K. Terakura, Phys. Rev. Lett. **80**, 5758 (1998).

[88] I. V. Solovyev, Phys. Rev. Lett. **95**, 267205 (2005).

[89] V. I. Anisimov, J. Zaanen, and O. K. Andersen, Phys. Rev. B **44**, 943 (1991).

[90] A. I. Lichtenstein, M. I. Katsnelson, and G. Kotliar, Phys. Rev. Lett. **87**, 067205 (2001).

[91] S. Chadov, J. Minár, H. Ebert, A. Perlov, L. Chioncel, M. I. Katsnelson, and A. I. Lichtenstein, Phys. Rev. B **74**, R140411 (2006).

[92] W. Grange, I. Galanakis, M. Alouani, M. Maret, J. P. Kappler, and A. Rogalev, Phys. Rev. B **62**, 1157 (2000).

[93] S. Biermann, A. Dallmeyer, C. Carbone, W. Eberhardt, C. Pampuch, O. Rader, M. Katsnelson, and A. Lichtenstein, JETP Letters **80**, 612 (2004), 10.1134/1.1851645.

[94] V. L. Moruzzi and P. M. Marcus, Phys. Rev. B **48**, 16106 (1993).

[95] A. F. Guillermet and G. Grimvall, Phys. Rev. B **40**, 1521 (1989).

[96] S. Chadov, G. H. Fecher, C. Felser, J. Minár, J. Braun, and H. Ebert, J. Phys. D: Appl. Phys. **42**, 084002 (2009).

[97] J. Kübler, A. R. William, and C. B. Sommers, Phys. Rev. B **28**, 1745 (1983).

[98] B. Balke, G. H. Fecher, H. C. Kandpal, C. Felser, K. Kobayashi, E. Ikenaga, J.-J. Kim, and S. Ueda, Phys. Rev. B **74**, 104405 (2006).

[99] H. C. Kandpal, G. H. Fecher, C. Felser, and G. Schönhense, Phys. Rev. B **73**, 094422 (2006).

[100] A. Koga, N. Kawakami, T. M. Rice, and M. Sigrist, Phys. Rev. B **72**, 045128 (2005).

[101] U. Fano, Phys. Rev. **178**, 131 (1969).

[102] J. Minár, H. Ebert, G. Ghiringhelli, O. Tjernberg, N. B. Brookes, and L. H. Tjeng, Phys. Rev. B **63**, 144421 (2001).

[103] C. De Nadaï, J. Minár, H. Ebert, G. Ghiringhelli, A. Tagliaferri, and N. B. Brookes, Phys. Rev. B **70**, 134409 (2004).

[104] W. Eberhardt, E. W. Plummer, K. Horn, and J. Erskine, Phys. Rev. Lett. **45**, 273 (1980).

[105] M. M. Steiner, R. C. Albers, and L. J. Sham, Phys. Rev. B **45**, 13272 (1992).

[106] A. Chainani, T. Yokoya, T. Kiss, and S. Shin, Phys. Rev. Lett. **85**, 1966 (2000).

[107] F. Reinert, G. Nicolay, B. Eltner, D. Ehm, S. Schmidt, S. Hüfner, U. Probst, and E. Bucher, Phys. Rev. Lett. **85**, 3930 (2000).

[108] S. Tsuda, T. Yokoya, T. Kiss, Y. Takano, K. Togano, H. Kito, H. Ihara, and S. Shin, Phys. Rev. Lett. **87**, 177006 (2001).

[109] F. Reinert, B. Eltner, G. Nicolay, D. Ehm, S. Schmidt, and S. Hüfner, Phys. Rev. Lett. **91**, 186406 (2003).

[110] G. Grimvall, *The electron-phonon interaction in metals* (North-Holland, Amsterdam, 1981).

[111] B. Hellsing and A. E. E. V. Chulkov, J. Phys.: Cond. Mat. **14**, 5959 (2002).

[112] S. Mankovsky and H. Ebert, Phys. Rev. B unpublished (2010).

[113] J. Minár, J. Braun, S. Mankovsky, and H. Ebert, J. Electron. Spectrosc. Relat. Phenom. submitted (2010).

[114] H. Cercellier, C. Didiot, Y. Fagot-Revurat, B. Kierren, L. Moreau, D. Malterre, and F. Reinert, Phys. Rev. B **73**, 195413 (2006).

[115] B. Eltner, Ph.D. thesis, Universität des Saarlandes, Saarbrücken, 2005.

[116] H. Dürr, J. Minár, A. Varykhalov, J. Braun, and H. Ebert, Unpublished (2010).